A&A, 694, A167 (2025)
https://doi.org/10.1051/0004-6361/202452061

Astronomy & Astrophysics

The Solar System's passage through the Radcliffe wave during the middle Miocene

E. Maconi[1,⋆], J. Alves[1], C. Swiggum[1], S. Ratzenböck[1,2], J. Großschedl[1,3,4], P. Köhler[5], N. Miret-Roig[1], S. Meingast[1], R. Konietzka[6], C. Zucker[6], A. Goodman[6], M. Lombardi[7], G. Knorr[5], G. Lohmann[5,8], J. C. Forbes[9], A. Burkert[10], and M. Opher[11,12]

[1] University of Vienna, Department of Astrophysics, Türkenschanzstraße 17, 1180 Wien, Austria
[2] University of Vienna, Research Network Data Science at Uni Vienna, Kolingasse 14–16, 1090 Vienna, Austria
[3] I. Physikalisches Institut, Universität zu Köln, Zülpicher Str. 77, 50937 Köln, Germany
[4] Astronomical Institute of the Czech Academy of Sciences, Boční II 1401, 141 31 Prague, Czech Republic
[5] Alfred-Wegener-Institut Helmholtz-Zentrum für Polar- und Meeresforschung, 27570 Bremerhaven, Germany
[6] Harvard University Dep. of Astronomy and Center for Astrophysics | Harvard & Smithsonian, Cambridge, MA, USA
[7] Università degli Studi di Milano, Dipartimento di Fisica, Via Celoria 16, 20133 Milano, Italy
[8] Department of Environmental Physics and MARUM, University of Bremen, Bremen, Germany
[9] School of Physical and Chemical Sciences, Te Kura Matū, University of Canterbury, Christchurch 8140, New Zealand
[10] University of Munich, Physics Department, Scheinerstrasse 1, 81679 Muenchen, Germany
[11] Radcliffe Institute for Advanced Studies at Harvard University, Cambridge, MA, USA
[12] Astronomy Department, Boston University, Boston, MA 02215, USA

Received 30 August 2024 / Accepted 8 January 2025

ABSTRACT

Context. As the Solar System orbits the Milky Way, it encounters various Galactic environments, including dense regions of the interstellar medium (ISM). These encounters can compress the heliosphere, exposing parts of the Solar System to the ISM, while also increasing the influx of interstellar dust into the Solar System and Earth's atmosphere. The discovery of new Galactic structures, such as the Radcliffe wave, raises the question of whether the Sun has encountered any of them.
Aims. The present study investigates the potential passage of the Solar System through the Radcliffe wave gas structure over the past 30 million years (Myr).
Methods. We used a sample of 56 high-quality, young (≤30 Myr) open clusters associated with a region of interest of the Radcliffe wave to trace its motion back and investigate a potential crossing with the Solar System's past orbit.
Results. We find that the Solar System's trajectory intersected the Radcliffe wave in the Orion region. We have constrained the timing of this event to between 18.2 and 11.5 Myr ago, with the closest approach occurring between 14.8 and 12.4 Myr ago. Notably, this period coincides with the Middle Miocene climate transition on Earth, providing an interdisciplinary link with paleoclimatology. The potential impact of the crossing of the Radcliffe wave on the climate on Earth is estimated. This crossing could also lead to anomalies in radionuclide abundances, which is an important research topic in the field of geology and nuclear astrophysics.

Key words. ISM: kinematics and dynamics – open clusters and associations: general – solar neighborhood

1. Introduction

As our Solar System orbits the Milky Way, it encounters different Galactic environments with varying interstellar densities, including hot voids, supernova (SN) blast wave fronts, and cold gas clouds. The Sun's passage through a dense region of the interstellar medium (ISM) may impact the Solar System in several ways (Fields & Wallner 2023; Opher et al. 2024a). For instance, the enhancement of the ram pressure compresses the heliosphere, exposing some parts of the Solar System to the cold and dense ISM (Miller & Fields 2022; Miller et al. 2024; Opher et al. 2024a,b). Additionally, the amount of interstellar dust loaded into Earth's atmosphere would increase, potentially enhancing the delivery of radioisotopes contained in the ISM gas, such as ^{60}Fe, via dust grains (see e.g., Altobelli et al. 2005; Breitschwerdt et al. 2016; Schulreich et al. 2017, 2023). This could cause geological radionuclide anomalies (Koll et al. 2019; Wallner et al. 2015, 2021). Moreover, an increased amount of dust within the Solar System might alter Earth's radiation budget, resulting in a cooling effect (see e.g., Shapley 1921; Talbot & Newman 1977; Pavlov et al. 2005). Therefore, it is crucial to investigate which Galactic environment was encountered by the Sun over its path.

Understanding the solar neighborhood, with its structures and the physical processes occurring within it, is thus of critical importance. Historically, this understanding has relied on plane-of-the-sky observations – meaning 2D (l–b) or pseudo-3D projections (l–b–v_R) of the actual underlying 3D structure. However, a new era in astronomy has begun with ESA's *Gaia* mission (Gaia Collaboration 2016). The astrometric data from *Gaia*, complemented with the spectroscopic information on the radial velocity of stars obtained by *Gaia* itself and other previous surveys such as LAMOST, RAVE, GALAH, and SDSS (Luo et al. 2015; Majewski et al. 2017; Steinmetz et al. 2020; Buder et al. 2021; Abdurro'uf et al. 2022), have opened a new 6D window into the stellar content of the Milky Way and a new understanding of the local ISM. Advanced statistical techniques have enabled the creation of 3D dust maps, extending up to

⋆ Corresponding author; efrem.maconi@univie.ac.at

several kiloparsecs from the Sun and achieving parsec-scale resolution for the nearby environment (see e.g., Green et al. 2019; Leike et al. 2020; Lallement et al. 2019, 2022; Vergely et al. 2022; Edenhofer et al. 2024). The analysis of *Gaia*-era 3D dust maps and molecular clouds' catalogs solely based on 3D positional data (see e.g., Zucker et al. 2019; Chen et al. 2020b; Dharmawardena et al. 2023; Cahlon et al. 2024) has unveiled structures such as the Radcliffe wave (Alves et al. 2020) and the Split (Lallement et al. 2019), which were previously thought to constitute a ring-like structure around the Sun, named the Gould Belt (Gould 1874), due to misleading projection effects.

In this paper, we investigate the possible encounter between the Sun and the Radcliffe wave. The Radcliffe wave (Alves et al. 2020) is a narrow (aspect ratio of 1:20) and coherent ∼2.7-kpc-long sinusoidal gas structure, which comprises many known star-forming cloud complexes, such as CMa, Orion, Taurus, Perseus, Cepheus, North America nebula, and Cygnus. This gas structure, with an estimated mass of $3 \cdot 10^6$ $M_\odot$, appears to coherently oscillate like a traveling wave (Konietzka et al. 2024) and it is thought to be part of the Galaxy spiral structure (Swiggum et al. 2022). We used recent open cluster catalogs to identify a subset of young (≤30 Myr), open clusters associated with the Radcliffe wave. By leveraging the new information regarding the 3D structure of the local ISM and the 3D spatial motions of the selected open clusters, used as tracers of the motion of the primordial clouds out of which they were born, we investigate potential interactions of our Solar System and the Radcliffe wave. Additionally, we discuss the possible geological signatures and climate effects that such an interaction could produce.

This paper is organized as follows. In Sect. 2, we outline the data used for the study. In Sect. 3, we describe the selection of the Radcliffe wave clusters, the estimation of their properties, such as age and mass, along with the properties of their parental clouds, and the method for orbit integration. We discuss the results and their interdisciplinary connections with other fields of study in Sect. 4 and we summarize our findings in Sect. 5.

2. Data

The Galactic cartesian coordinates (*X*, *Y*, *Z*) of the molecular clouds constituting the Radcliffe wave structure are taken from the studies by Zucker et al. (2019) and Alves et al. (2020). The molecular clouds catalog by Zucker et al. (2019) was constructed using a Bayesian statistical method, incorporating optical and near-infrared photometry, along with astrometric data, from the Pan-STARRS survey (Chambers et al. 2019; Flewelling et al. 2020), the 2MASS survey (Skrutskie et al. 2006), the NOAO source catalog (Nidever et al. 2018), and parallaxes from the second *Gaia* Data Release (Arenou et al. 2018; Gaia Collaboration 2018). We used the positions of the clouds that constitute the Radcliffe wave to identify young clusters that may be associated with it.

For the clusters, we primarily used the recent open star cluster catalog by Hunt & Reffert (2023) (hereafter, HR23). This catalog was constructed by applying the Hierarchical Density-Based Spatial Clustering of Applications with Noise routine (McInnes et al. 2017) (HDBSCAN) on the *Gaia* DR3 astrometrical data (Gaia Collaboration 2023) and the results were validated through a statistical density test and a Bayesian convolutional neural network. The catalog comprises a total of 7166 star clusters and provides a broad array of parameters. Of particular importance for our research are the sky positions, parallaxes, proper motions, radial velocities (RVs), estimated ages, extinctions, and stellar membership lists. To get better statistics for the full 6D phase space, we added additional RV data to the existing *Gaia* DR3 RVs. We cross-matched the stellar members of each cluster to the following surveys: APOGEE-2 SDSS DR17 (Abdurro'uf et al. 2022), GALAH DR3 (Buder et al. 2021), RAVE DR6 (Steinmetz et al. 2020), *Gaia* ESO DR6 (Randich et al. 2022), LAMOST DR5 (Zhao et al. 2012; Tsantaki et al. 2022), and two RV compilations (Gontcharov 2006; Torres et al. 2006). In cases where a star is present in multiple surveys, we selected the RV value with the lowest uncertainty. Before recomputing the clusters' median RVs, we first excluded stars with RV errors greater than 5 km s^{-1} and, secondly, we applied sigma-clipping using 3-sigma around the cluster median. To further ensure the accuracy of our results, we imposed a minimum requirement of at least five stars used in the computation of each cluster's median RV and we considered only those clusters with RV errors below 3 km s^{-1}. Clusters that have only three or four stellar members with RVs were included again if the standard error is below 1.2 km s^{-1}, since these show a very narrow distribution in RV space. We then computed each cluster's mean Galactic cartesian velocities (*U*, *V*, *W*) and the corresponding standard error (see Table A.1). To ensure the positional accuracy of our results, we considered only those clusters with positional errors below 50 pc for the *XYZ* positions. Subsequently, we checked that none of the discarded clusters held relevance for our findings. Moreover, we compared our selection to the one used in a recent paper that investigated the Radcliffe wave's motions (Konietzka et al. 2024). In that study, the authors used a compilation of several cluster catalogs (Sim et al. 2019; Liu & Pang 2019; Cantat-Gaudin et al. 2020; Szilágyi et al. 2021; Hao et al. 2022; He et al. 2022) that predated HR23. We found that seven clusters of relevance to this study were missing from our selection. We computed the median positions and velocities of these additional clusters using the membership lists from the auxiliary cluster catalogs and cross-matches with the mentioned RV catalogs, deploying the same procedure as outlined above. As a result, four additional clusters passed our quality check: CWNU 1028, NGC 1977, OC 0340, and UBC 207. The Galactic positions and velocities of the clusters, reported in Table A.1, were then used to integrate their orbits in the past. More information are provided in Sect. 3.

3. Methods

3.1. Identification of the Radcliffe wave's clusters

We identified the clusters that could be associated with the Radcliffe wave by using the catalog of molecular clouds that constitute this structure (Alves et al. 2020) and the cluster sample described in Sect. 2. As a first step, we considered the clusters that, at the present day, are within 60 pc to the major molecular clouds and tenuous gas connections comprising the Radcliffe wave. We opted for this conservative threshold, as the radius of the Radcliffe wave has been estimated to be around 50 pc by Konietzka et al. (2024). Extending the threshold to 60 pc accounts for positional uncertainties that might bring clusters into this range. We chose not to include clusters farther away as their connection to the Radcliffe wave would be more uncertain. Additionally, we investigated the clusters that are located between 60 and 100 pc, and we verified that they are not relevant to our results. Using this distance criterion, we initially selected 104 clusters. As a second step, since we are interested in relatively young clusters whose motion may still be related to the gas phase of the Radcliffe wave, we applied an age cut and only considered those with an age estimate smaller than

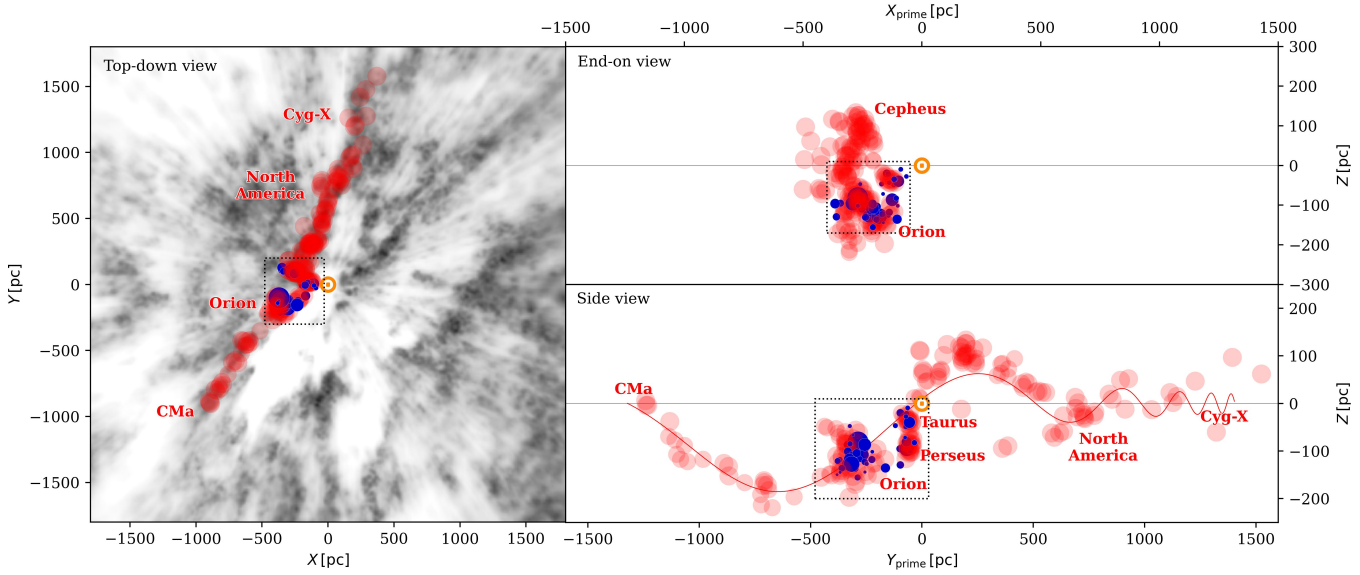

Fig. 1. Overview of the Radcliffe wave and selected clusters, in a heliocentric Galactic Cartesian frame. The Sun is placed at the center and its position is marked with a golden-yellow ⊙. The red dots denote the molecular clouds and tenuous gas bridge connections that constitute the Radcliffe wave (Zucker et al. 2019; Alves et al. 2020). The blue points represent the 56 open clusters associated with the region of the Radcliffe wave that is relevant for this study. The size of the circles is proportional to the number of stars in the clusters. In the XY-plane on the left panel, the gray scale represents a dust map (Vergely et al. 2022) of the solar neighborhood integrated over the z-axis. To properly visualize the Radcliffe wave's structure, the XY-plane has been rotated counterclockwise by 120° for the $ZX_{\rm prime}$-plane (top-right panel) and by 30° for the $ZY_{\rm prime}$-plane (bottom-right panel), for an observer facing the Galactic anticenter. In the $ZY_{\rm prime}$-plane, the red-solid line represents the Radcliffe wave's best fit model (Konietzka et al. 2024).

30 Myr. We computed the ages of the clusters using the *Gaia* DR3 photometry, employing the procedure described in Sect. 3.2 and Appendix A.1. After applying the age cut, we were left with a total of 74 clusters that we consider to be associated with the Radcliffe wave. As a final selection step, we did a preliminary orbit integration over the past 30 Myr (for the integration details, see Sect. 3.4) to check which clusters come closer than 300 pc to the Sun in this time frame. This left us with a sample of 56 clusters.

In Fig. 1, we show the present-day positions of the 56 identified clusters, along with the molecular clouds comprising the Radcliffe wave. The heliocentric positions and velocities of the clusters are listed in Table A.1. The selected clusters belong to the Taurus, Perseus, and Orion star-forming regions of the Radcliffe wave (see Table A.2). The cluster names used in this work are listed in Table A.2. We primarily use the names from the assembled cluster catalogs, while we have renamed some of the selected clusters with their previously defined and more widely recognized names, in cases where a significant cross-match of their stellar members aligns with those of previous studies (Chen et al. 2020a; Pavlidou et al. 2021; Krolikowski et al. 2021).

We used the 3D positions and velocities of the selected clusters to estimate their past orbits in the Milky Way as well as the previous orbits of the molecular clouds out of which they formed. The past positions of the gas clouds were inferred from the pre-birth trajectories of the clusters associated with them. This is based on the momentum conservation principle, which implies that the velocities of newly formed and young clusters are correlated with those of the center of mass of the natal gas (see e.g., Fernández et al. 2008; Tobin et al. 2009; Hacar et al. 2016; Großschedl et al. 2021; Konietzka et al. 2024). As the trajectories of these clusters appear to be interconnected rather than independent, exhibiting common motion (see also Sect. 4.1), and as they are all part of the Radcliffe wave, we interpret the orbits of their natal clouds as tracers of a larger gas complex. In this view, the gas clouds should not be considered as isolated objects but rather as parcels of a bigger gas structure. The fragmentation of this structure produced several bound, dense gas clumps where the analyzed star clusters subsequently formed. For simplicity, we adopt this decomposition into distinct "clouds" and refer to these parcels of gas as clouds throughout the paper. Notable examples within the analyzed region include the Orion A and Orion B giant molecular clouds, which extend for about 200 pc, each containing many embedded clusters. We acknowledge that this modeling approach simplifies the real structure and evolution of the gas clouds, but it is the only one applicable in this case since the exact shape of a cloud in the past cannot be recovered, as the gas is not rigid and its distribution is influenced by multiple mechanisms (see also Sect. 3.3). Considering these systematic uncertainties, the trajectories of the clusters and their parental clouds should be considered as preliminary estimates of the actual cloud paths. We refer the reader to Sects. 3.2, 3.3, and 3.4, for more details on the properties of the clusters, the properties of the parental clouds, and the orbit integration, respectively.

3.2. Estimation of ages and masses of the Radcliffe wave's clusters

In this paper, we mainly used the HR23 cluster catalog, which already provides a homogeneous estimate of cluster ages and extinctions, using an approximate Bayesian neural network model which was trained on simulated data. However, as the age estimation was not the main focus of that paper, we recomputed the ages with a more robust and slightly more computationally expensive method. This method uses the recently developed `Python` package `Chronos` (see Ratzenböck et al. 2023b, for more details), which is capable of estimating the age, extinction,

and metallicity of a cluster by performing a Bayesian fit of each cluster's stellar members to theoretical model isochrones. We decided to use the PARSEC models (Bressan et al. 2012; Nguyen et al. 2022) in combination with *Gaia* DR3 photometry. We assumed the clusters to have the same metallicity, as they are young (≤30 Myr) and spatially close. We adopted a solar metallicity, since the chemical composition of Radcliffe wave clusters has been shown to be compatible with that of the Sun (see e.g., Alonso-Santiago et al. 2024). We also recomputed the ages for the clusters not present in HR23 (see Sect. 2 for more details). In Table A.2, we report the estimated ages for the 56 clusters of the Radcliffe wave that we are considering in this work. In Fig. A.1 and A.2, we show the color-magnitude diagrams that are used for isochrone fitting. In Fig. A.3, we compare the ages of the clusters computed in this work with the ones provided by the source catalogs. We refer the reader to Appendix A.1 for more details.

We estimated the mass of a given cluster by summing the masses of its stellar members, which were determined from the isochrone fitted by `Chronos`. To correct for the incompleteness of the cluster's members, possibly due to observational limits or stellar evolution, we compared the measured mass distributions to the initial mass function (IMF) by Kroupa (2001). By minimizing the total mass difference between a given IMF and the inferred one, we obtained the IMF that best fits our data. This minimization was performed within the mass range of 0.3 and 2 $M_\odot$, which is determined by the completeness limits of *Gaia* data (Meingast et al. 2021; Gaia Collaboration 2023). The low-mass end limit of the Kroupa IMF was set to 0.03 $M_\odot$, to account for objects that are below the hydrogen-burning limit. We did not specify a high-mass bound to account for potentially missing massive sources that are either too bright for *Gaia* or have undergone SN explosion. In Table A.2, we list the total masses of the clusters obtained by summing the masses of their members and those derived from the best-fit mass functions. In Fig. A.4, we show the best-fit mass functions, together with the inferred ones, for each of the clusters under analysis.

The reported cluster masses should be regarded as lower limits. This is due to various uncertainties, including the limitations of the HDBSCAN clustering algorithm. These limitations also subsequently affect the cloud radii and estimated number of SN (see Sect. 3.3 and Appendix A.3). The HDBSCAN algorithm indeed may not select all stellar members of each cluster, even if a star falls within a mass range where *Gaia* data is considered complete. This issue is inherent to all clustering algorithms, as they operate based on their own assumptions that may not fully encompass the wide range of cluster shapes, densities, and sizes. The presence of this systematic bias becomes evident when comparing different solutions from various clustering methods and attempts within the same region (see Ratzenböck et al. 2023a, for details).

3.3. Properties of the parental clouds associated with the clusters

For the times preceding the birth of a given cluster during the orbital tracebacks, we assumed the primordial clouds of the Radcliffe wave to have an onion-like structure. Each cloud was modeled as a set of concentric spheres with radii of 20, 30, 40, and 50 pc, representing the denser central parts and lower-density outskirts of each cloud. This modeling approach allows us to simplify the complex and varied structures exhibited by gas clouds. Indeed, molecular gas is typically organized into distinct, filamentary clouds (see e.g., André et al. 2010; Molinari et al. 2010; Li et al. 2013; Zucker et al. 2018; Imara & Forbes 2023) arranged hierarchically, ranging from giant complexes spanning up to 100 pc, down to smaller, denser cores of few parsec in size (see e.g., Ferrière 2001; Motte et al. 2018). These clouds can be surrounded by more diffuse gas (see e.g., Snow & McCall 2006) and are constantly influenced by various physical mechanisms acting on different scales. These mechanisms include Galactic mechanisms (see e.g., Inutsuka et al. 2015), stellar feedback (see e.g., Walch & Naab 2015; Großschedl et al. 2021; Posch et al. 2023), and magnetic fields (see e.g., Hennebelle & Inutsuka 2019). Our approach is thus motivated by the fact that we cannot determine the past shapes of the clouds from the data.

In addition to the onion structure modeling, which aims to include the extension of both the tenuous gas and the central parts of the parental clouds associated with the clusters, we computed an estimate of the mass and radius of the densest part ($n_H \geq 40\,\mathrm{cm}^{-3}$) of the gas clouds. We estimated the mass of the gas cloud associated with a given cluster (M_{cloud}) as

$$M_{\mathrm{cloud}} = \frac{M_{\mathrm{stars}}}{\mathrm{SFE}}, \tag{1}$$

where M_{stars} is the stellar mass of the cluster corrected for incompleteness, as described in the Sect. 3.2, and SFE is the star formation efficiency for the Radcliffe wave, which is assumed to vary between 1% and 3% (see e.g., Kennicutt & Evans 2012; Swiggum et al. 2022), though higher values have also been reported for the SFE in molecular clouds (see e.g., Chevance et al. 2020).

We used a mass-size relation to estimate the radius of an equivalent sphere with the same mass as our estimated cloud masses. Such relations have been studied both observationally and numerically, starting with the work of R.B. Larson (Larson 1981), which was recently updated with the help of *Gaia* data, delivering a new 3D perspective for molecular clouds (see also Sect. 1). It has been found (Cahlon et al. 2024) that the masses of the clouds scale in relation to their volume ($M_{\mathrm{cloud}} \propto r^3_{\mathrm{cloud}}$) when 3D data are used, whereas they scale with the area ($M_{\mathrm{cloud}} \propto r^2_{\mathrm{cloud}}$) when the 3D data are projected onto a 2D plane. This is consistent with the predictions of previous theoretical and numerical studies (see e.g., Shetty et al. 2010; Beaumont et al. 2012; Ballesteros-Paredes et al. 2019). Therefore, we estimated the radius of the densest part for the parental clouds using the observationally based 3D mass-size relation from Cahlon et al. (2024),

$$M_{\mathrm{cloud}}(r) = 7\,M_\odot \left(\frac{r}{\mathrm{pc}}\right)^{2.9}. \tag{2}$$

We list the resulting cloud radii and masses in Table A.2. By assuming a SFE of 1% (3%), the estimated masses of the clouds span from $1.44 \times 10^5\,M_\odot$ ($0.48 \times 10^5\,M_\odot$) for lambda-Ori to $750\,M_\odot$ ($250\,M_\odot$) for L1546. The corresponding estimated radii for these clouds are 30.7 pc (21.0 pc) and 5.0 pc (3.4 pc), respectively. As outlined in Sect. 3.2, the cloud radii and masses are likely underestimated and should be considered as lower limits, resulting from the incompleteness of stellar members in the cluster catalogs.

3.4. Orbit integration

We estimated the past orbits of the clusters, the associated clouds, and the Sun using the Galactic dynamics package `galpy` (Bovy 2015) in combination with the `Astropy` package (Astropy Collaboration 2022). `galpy` offers the possibility to numerically

integrate orbits over different Milky Way potentials and initial conditions, such as the Galactocentric distance, the Sun's height above the disk mid-plane, and the Sun's velocity.

For our study, we used `galpy`'s `MWPotential2014` as a model for the Milky Way's gravitational potential. This model includes a bulge, a disk, and a halo component that are modeled as a power-law density profile with an exponential cut-off, a Miyamoto-Nagai potential, and a Navarro–Frenk–White profile, respectively (see Bovy 2015, for details). We assumed a solar Galactocentric radius of $R_\odot = 8.33$ kpc (Gillessen et al. 2009) and a vertical position of $z_\odot = 27$ pc (Chen et al. 2001). The Sun's velocity relative to the Local Standard of Rest, whose circular velocity is set to the default `galpy` value of 220 km s^{-1}, is $(U_\odot, V_\odot, W_\odot) = (11.1, 12.24, 7.25)$ km s^{-1} (Schönrich et al. 2010). These parameters are internally used by `galpy` to change the reference frame from the Sun's coordinate system to the Galactic center's coordinate system before performing the orbit integration. The initial positions and velocities of the clusters, defined using the `Astropy` package, serve as input for `galpy`'s orbit module. Our integration covered the past 30 Myr, with a time-step of 0.03 Myr. We employed `galpy`'s `dop853-c` method, a Dormand-Prince integrator known for its reliability and speed.

We addressed the statistical uncertainties in the positions and velocities of the Sun and clusters by integrating their orbits 1000 times, each using new sets of data obtained by sampling the uncertainty distribution with a Monte Carlo sampling method. The initial positions and velocities of the considered clusters with respect to the Sun, along with the errors, are listed in Table A.1, while the errors on the solar parameters are sourced from the provided references. Being aware of the fact that there is not a unique definition of the solar parameters and of the Milky Way potential, in Appendix B we tested the effect that different initial conditions have on our results. We conclude that the past trajectories of the Sun and the clusters, and their relative distances, do not significantly vary over the last 30 Myr when altering the described parameters. This can be attributed to the relatively short integration time considered, as found from prior studies (see e.g., Miret-Roig et al. 2020), and supports the robustness of our conclusions.

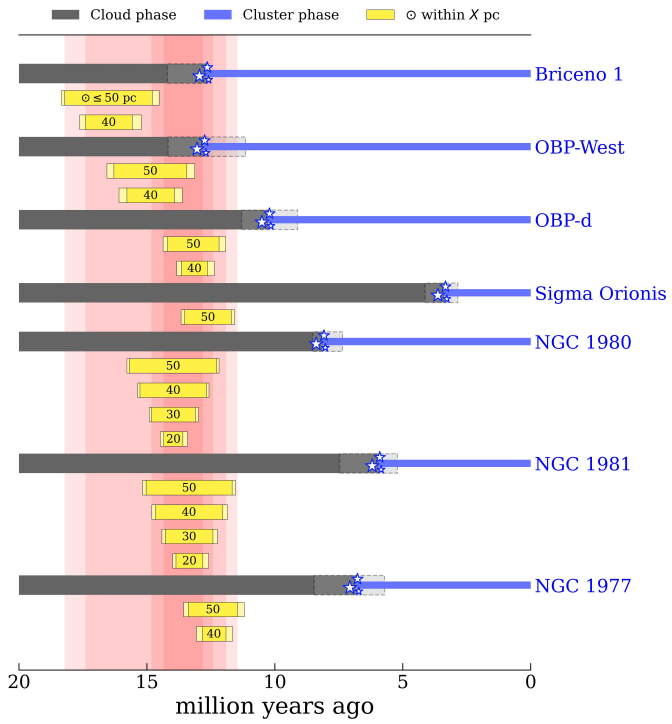

Fig. 2. Significant encounters between the Solar System and the clusters of the Radcliffe wave during their cloud phase in the past 30 Myr, considering various threshold distances ($d_{\mathrm{Sun-cloud}}$; 50, 40, 30, and 20 pc). For each cluster, the cloud phase is represented by a horizontal gray band, the moment at which the cluster is formed is highlighted by three small stars, and the time period during which the cluster is fully formed (gas free phase) is denoted by a blue band. The age range of the cluster, as computed in this work, is indicated by a light-gray band with a dashed edge. The yellow bands highlight the time period during which the Solar System is within a certain distance from the clouds. Light-yellow represents the statistical uncertainty of the crossing times, as computed from the tracebacks. The vertical red stripes summarize the time range during which the Solar System is passing through the gaseous part of the Radcliffe wave. The closer the transit, the redder the vertical stripe. The numerical equivalent of this plot is reported in Table 1.

4. Results and discussion

4.1. Solar System's crossing of the Radcliffe wave

To assess a potential crossing of the Radcliffe wave by the Solar System, we computed, at each time step of the orbits tracebacks, the distances between the Sun and the clusters. For time intervals preceding the age of a given cluster, we considered its pre-birth trajectory as a first approximation of the orbit of the primordial cloud associated with it. As described in Sect. 3.1, we interpret the motion of the analyzed clouds as tracing the motion of the larger gas complex they belong to. By computing the time ranges in which the Sun and the center of the parental gas clouds are closer than their radii – considered as threshold distances – we were able to determine when the Sun most likely crossed these clouds and consequently the Radcliffe wave. We deemed a crossing significant if its probability of occurrence exceeds 50%. This was computed by repeating the tracebacks of the orbits multiple times, as described in Sect. 3.4.

Remarkably, we find that the past trajectories of the Solar System closely approached ($d_{\mathrm{Sun-cloud}}$ within 50 pc) certain selected clusters while they were in their cloud phase, hinting at a probable encounter between the Sun and the gaseous component of the Radcliffe wave. When considering a cloud as a sphere of gas spanning 50 pc, we observe that the Sun's orbit was concurrently passing through multiple parental clouds associated with the clusters Briceno 1, OBP-West, OBP-d, Sigma Orionis, NGC 1980, NGC 1981, and NGC 1977 between 18.2 ± 0.1 and 11.5 ± 0.3 Myr ago. These clusters are currently located within the Orion star-forming complex. It is relevant and interesting to note, from a historical perspective, that a possible crossing of the Orion region by the Solar System was already suggested by Shapley (1921), based on much less reliable data. Assuming a threshold distance of 40 pc, the Sun would still cross the gas clouds of all these clusters, with the exception of Sigma Orionis, approximately from 17.4 ± 0.2 to 11.9 ± 0.3 Myr ago. Considering 30 pc and 20 pc radii, the Solar System is within the parental clouds of NGC 1980 and NGC 1981 between 14.8 ± 0.1 and 12.4 ± 0.2 Myr ago, and 14.3 ± 0.1 and 12.8 ± 0.2 Myr ago, respectively. These time ranges are approximate since gravitational scattering from the clouds and stellar feedback are not accounted for; however, given the short integration times (less than 30 Myr; see e.g., Kamdar et al. 2021), the presented approximations are a valid first step to better understand the past Sun and clouds interactions.

The crossing time ranges of the Radcliffe wave by the Sun are shown in Fig. 2 and listed in Table 1. A complete animation

Table 1. Time ranges and statistical errors for significant encounters (crossing probability greater than 50%) between the Sun and the Radcliffe wave's clusters, assuming different threshold distances ($d_{\mathrm{Sun-cloud}}$).

Name	$d_{\mathrm{Sun-cloud}} \leq 50$ pc		$d_{\mathrm{Sun-cloud}} \leq 40$ pc		$d_{\mathrm{Sun-cloud}} \leq 30$ pc		$d_{\mathrm{Sun-cloud}} \leq 20$ pc	
	t_{enter} (Myr)	t_{exit} (Myr)	t_{enter} (Myr)	t_{exit} (Myr)	t_{enter} (Myr)	t_{exit} (Myr)	t_{enter} (Myr)	t_{exit} (Myr)
Briceno 1	-18.2 ± 0.1	-14.8 ± 0.3	-17.4 ± 0.2	-15.6 ± 0.4	–	–	–	–
OBP-West	-16.3 ± 0.3	-13.4 ± 0.3	-15.8 ± 0.3	-13.9 ± 0.3	–	–	–	–
OBP-d	-14.2 ± 0.2	-12.2 ± 0.3	-13.6 ± 0.2	-12.6 ± 0.3	–	–	–	–
Sigma Orionis	-13.5 ± 0.1	-11.7 ± 0.1	–	–	–	–	–	–
NGC 1980	-15.7 ± 0.1	-12.3 ± 0.1	-15.3 ± 0.1	-12.7 ± 0.1	-14.8 ± 0.1	-13.1 ± 0.1	-14.3 ± 0.1	-13.6 ± 0.2
NGC 1981	-15.0 ± 0.1	-11.7 ± 0.1	-14.7 ± 0.1	-12.0 ± 0.2	-14.3 ± 0.1	-12.4 ± 0.2	-13.9 ± 0.1	-12.8 ± 0.2
NGC 1977	-13.4 ± 0.2	-11.5 ± 0.3	-12.8 ± 0.2	-11.9 ± 0.3	–	–	–	–
Radcliffe wave	-18.2 ± 0.1	-11.5 ± 0.3	-17.4 ± 0.2	-11.9 ± 0.3	-14.8 ± 0.1	-12.4 ± 0.2	-14.3 ± 0.1	-12.8 ± 0.2

Notes. This table serves as the numerical complement to Fig. 2.

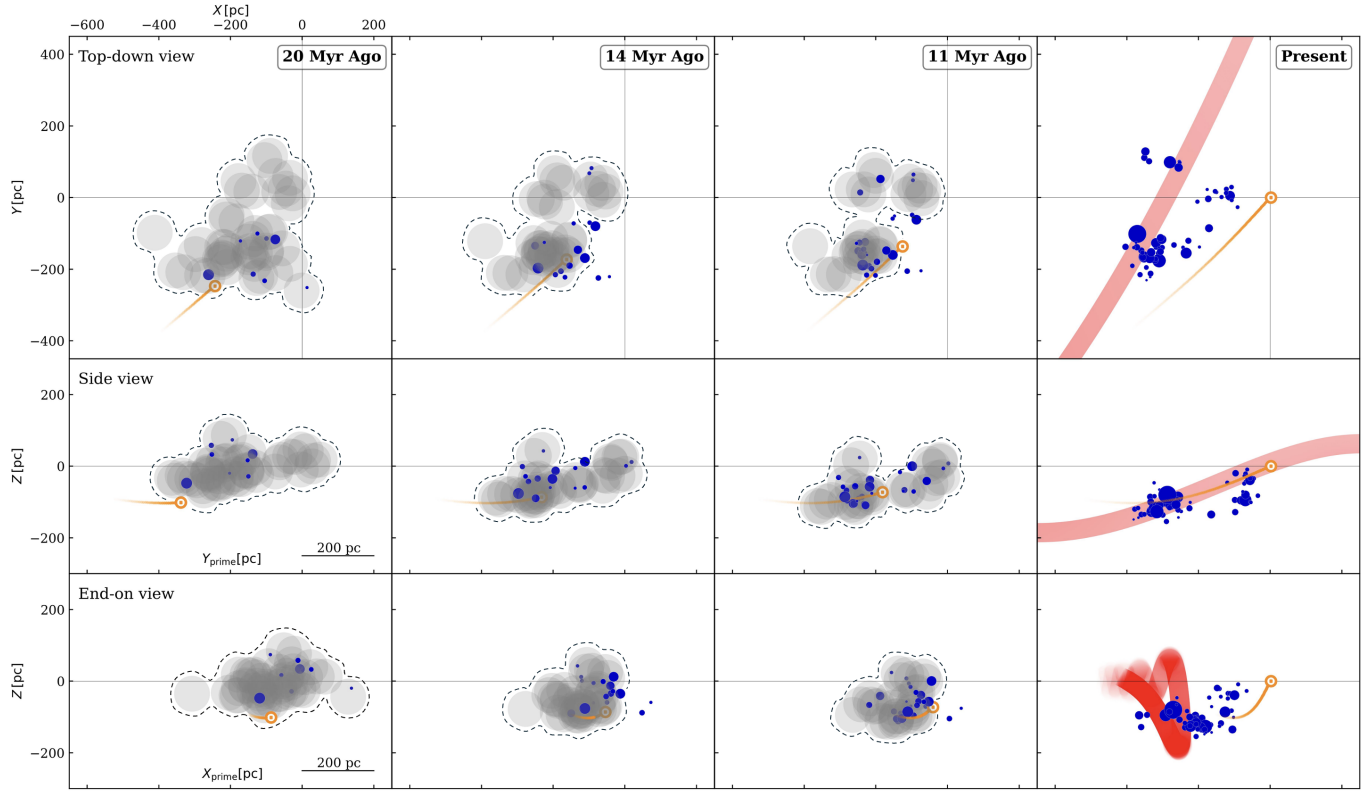

Fig. 3. Selected time snapshots for the tracebacks of the orbits of the Sun, selected clusters, and relative parental clouds. In the columns from left to right, we depict the Sun approaching the Radcliffe wave (t = 20 Myr ago), the Sun within the gas of the Radcliffe wave (t = 14 Myr ago), the Sun after it exited this gas structure (t = 11 Myr ago), and the present day situation (t = Present), respectively. The panels in the first row illustrate a top-down projection, while those in the second and third rows show side and end-on views, respectively, as depicted in Fig. 1. The Sun is denoted by a golden-yellow ⊙, and its trail is represented by dotted points with decreasing opacity. The analyzed clusters are indicated as blue circles, whose sizes are proportional to the number of their stellar members. Clusters prior to their birth are represented by light-gray circles, symbolizing 50 pc radius gas clouds. We enclosed the clouds with a dashed black line to highlight the larger gas complex they are part of. The best-fit model (Konietzka et al. 2024) of the Radcliffe wave is shown as a light-red band in the present day panels. An online 3D animation is available here, viewable from any angle and at any time step over the past 30 Myr.

illustrating the orbital trajectories of the clusters, clouds, and Sun over the past 30 Myr is presented in Fig. 3 (`interactive`). In the static version, we depict four different snapshots at −20 Myr, −14 Myr, −11 Myr, and the present. It can be seen that the Sun was approaching, crossing, and leaving the Radcliffe wave. In Fig. 3, we enclose the represented clouds with a dashed line, emphasizing the fact that they should be considered as part of a larger gas complex. From the interactive version of the figure, it is possible to note that the orbits of these clusters exhibit common motion. For some, their birthplaces likely indicate a shared formation history, although they do not need to come from exactly the same point in space. This is supported by the fact that some of the analyzed clusters belong to one of the three families of clusters identified in the work by Swiggum et al. (2024). For example, UPK 398, ASCC 18, ASCC 20, OCSN 64, OCSN 65, and CWNU 1072 are part of the Collinder 135 cluster family. Clusters in each of these three families converge toward each other when traced backward in time, consistent with

shared formation origins (see Swiggum et al. 2024, Extended Data Fig. 1). Additionally, previous studies have already examined most of these clusters in the context of Orion (see e.g., Bally et al. 1987; Brown et al. 1994; Briceno 2008; Alves & Bouy 2012; Chen et al. 2020a; Kounkel 2020; Großschedl et al. 2021).

For the seven clusters to which the Sun's orbits get closer than 50 pc with a high probability, the estimated radii of the densest parts of the associated gas clouds (densities higher than 40 particles per cm^3) range between 11.9–21.2 pc when considering 1% SFE, or 8.2–14.5 pc for a 3% SFE (refer to Sect. 3.3 and Table A.2). Especially noteworthy is the case of NGC 1980, one of the two clusters to which the Solar System approaches within 20 pc. For this cluster, we estimated a radius of 21.2 pc (14.5 pc), which further supports our crossing hypothesis. It is important to clarify that the estimated radii pertain to the densest part of the clouds, which can then be surrounded by tenuous gas enveloping the central regions (see e.g., Snow & McCall 2006). Moreover, these radii should be considered as lower limits, given the likely incompleteness of the cluster catalog, as previously highlighted in Sect. 3.3. We remark that these findings hold true even when assuming other initial conditions for the Sun's parameters and different Milky Way potentials (see Appendix B for details).

4.2. Interdisciplinary bridges: Potential geological and climate evidences

The crossing of a dense region of the ISM by the Sun, such as a gas cloud or a SN blast wave, can impact the Solar System in various ways (see e.g., Fields & Wallner 2023; Opher et al. 2024a). For example, the compression of the heliosphere by enhanced ram pressure exposes parts of the Solar System to the cold and dense ISM (see e.g., Miller & Fields 2022; Opher et al. 2024a,b). The amount of dust loaded into Earth's atmosphere would also increase, probably enhancing the delivery of radioisotopes (e.g., ^{60}Fe) via dust grains (see e.g., Altobelli et al. 2005; Breitschwerdt et al. 2016). This could lead to anomalies in geological radionuclide records (Koll et al. 2019; Wallner et al. 2015, 2021) and could provide evidence of the passage of the Sun through the Radcliffe wave. Our estimates suggest that the Orion region traversed by the Sun may have been enriched with radioisotopes from 3^{+1}_{-2} SN before 11.5 Myr ago, with the potential incompleteness of the stellar membership in the catalogs increasing this estimate. For the estimation of the number of past SN events, we refer to Appendix A.3. Although current ^{60}Fe data do not cover our period of interest (Fields & Wallner 2023), future instrumentation is expected to be sensitive enough to analyze this time period.

Furthermore, an increased amount of dust could impact Earth's radiation budget, potentially leading to a cooling effect (see e.g., Talbot & Newman 1977; Pavlov et al. 2005). Notably, our estimated time interval for the Solar System's potential location within a dense ISM region (about 14.8–12.4 Myr ago for a distance of 20–30 pc from the center of a gas cloud) overlaps with the Middle Miocene climate transition (Steinthorsdottir et al. 2021). During this period, the expansion of the Antarctic ice sheet (Miller et al. 2020) and global cooling (Westerhold et al. 2020) marked Earth's final transition to persistent large-scale continental glaciation in Antarctica (see Fig. 4, panels c, d and g, h). The ice sheet-climate interactions during the Miocene are complex (Knorr & Lohmann 2014; Stap et al. 2024) and the evolving understanding suggests that this cooling phase was possibly caused by falling atmospheric CO_2 concentrations (Cenozoic CO_2 Proxy Integration Project (CenCO_2PIP) Consortium 2023) (Fig. 4, panels b and f). However, CO_2 reconstructions beyond what is covered in Antarctic ice core data (the last 0.8 Myr) are highly uncertain (Fig. 4, panel a and e) and CO_2, when reconstructed from alkenones (van de Wal et al. 2011) (Fig. 4, panel e, light blue circles), seem indeed to suggest that the Middle Miocene cooling was not directly coupled to CO_2 radiative forcing. Therefore, it is intriguing to consider that the passage of our Solar System through a dense region of the ISM might have contributed to this climate transition, even if this remains speculative and currently lacks direct proof. We cautiously point out such possibilities to make the community aware of maybe overlooked processes, but we are conscious that available ^{60}Fe data do not extend beyond 10 Myr ago (Fields & Wallner 2023) and to our knowledge no rise in dust load has yet been discovered around 14 Myr ago in deep sea sediments (Rea 1994). Furthermore, the suggested decoupling of Middle Miocene temperature and alkenone-based CO_2, that opens up the possibility that not CO_2 but other processes are responsible for the reconstructed cooling, needs to be taken with caution, since recently various authors have suggested that some fundamental difficulties exist in studies that used alkenones for the reconstruction of atmospheric CO_2 (e.g., Phelps et al. 2021; Rae et al. 2021; Brandenburg et al. 2022).

We compared the radiative forcing and climate response during the Middle Miocene cooling period to what is known for the ice ages of the Pleistocene (2.6–0.01 Myr ago), in order to estimate by how much the extraterrestrial dust flux to Earth needs to have changed during the Solar System's crossing of the Radcliffe wave to serve as the primary driver of this climate transition – alternatively to atmospheric CO_2 concentrations. We based our analysis on the Pleistocene, as this period has a significantly more extensive data coverage. However, we acknowledge that this is an imperfect comparison, partly due to differences in the time scales of climate change (Myr in the Middle Miocene versus 10–100 kyr in the Pleistocene), and because the CO_2 radiative forcing changes during the Middle Miocene climate transition and late Pleistocene ice ages are of similar size, yet linked to different climate responses. Nonetheless, we used this comparison to obtain an order of magnitude estimate of the required change in dust flux.

During the Middle Miocene climate transition, the long-term mean radiative forcing of CO_2 shows a reduction by $\sim 2\,W\,m^{-2}$ (Fig. 4, panel f). Concurrently, the long-term and global mean surface temperature, estimated from benthic $\delta^{18}O$ (Fig. 4, panel g), decreased by more than 2 K (Westerhold et al. 2020) and sea level dropped by ~20 m (Fig. 4, panel h). We refer to Rohling et al. (2024) for the ongoing discussion on apparent discrepancies in reconstructed Cenozoic climate change based on different proxies. During glacial periods of the late Pleistocene, a similar reduction in CO_2 radiative forcing, together with other forcing and feedback processes (Köhler et al. 2010), led to a global mean surface cooling of approximately 6 K (Tierney et al. 2020; Clark et al. 2024) and to land ice sheets growth, mainly in North America and Eurasia. This ice sheets expansion corresponded to a sea level drop of about ~120 m (Gowan et al. 2021). The root cause of Pleistocene glaciations is understood to be the changes of Earth's orbital parameters (Milankovic 1941; Barker et al. 2025), which led to variations in incoming solar radiation (Laskar et al. 2004). Nevertheless, reduced greenhouse gas concentrations, increased atmospheric dust load, and higher surface albedo are important contributions necessary to drive Earth's climate into an ice age (Köhler et al. 2010).

During the late Pleistocene ice ages, the glacial dust (i.e., global dust during ice ages) deposition rate was 2–4 times larger than today (Albani et al. 2016; Mahowald et al. 2023) and,

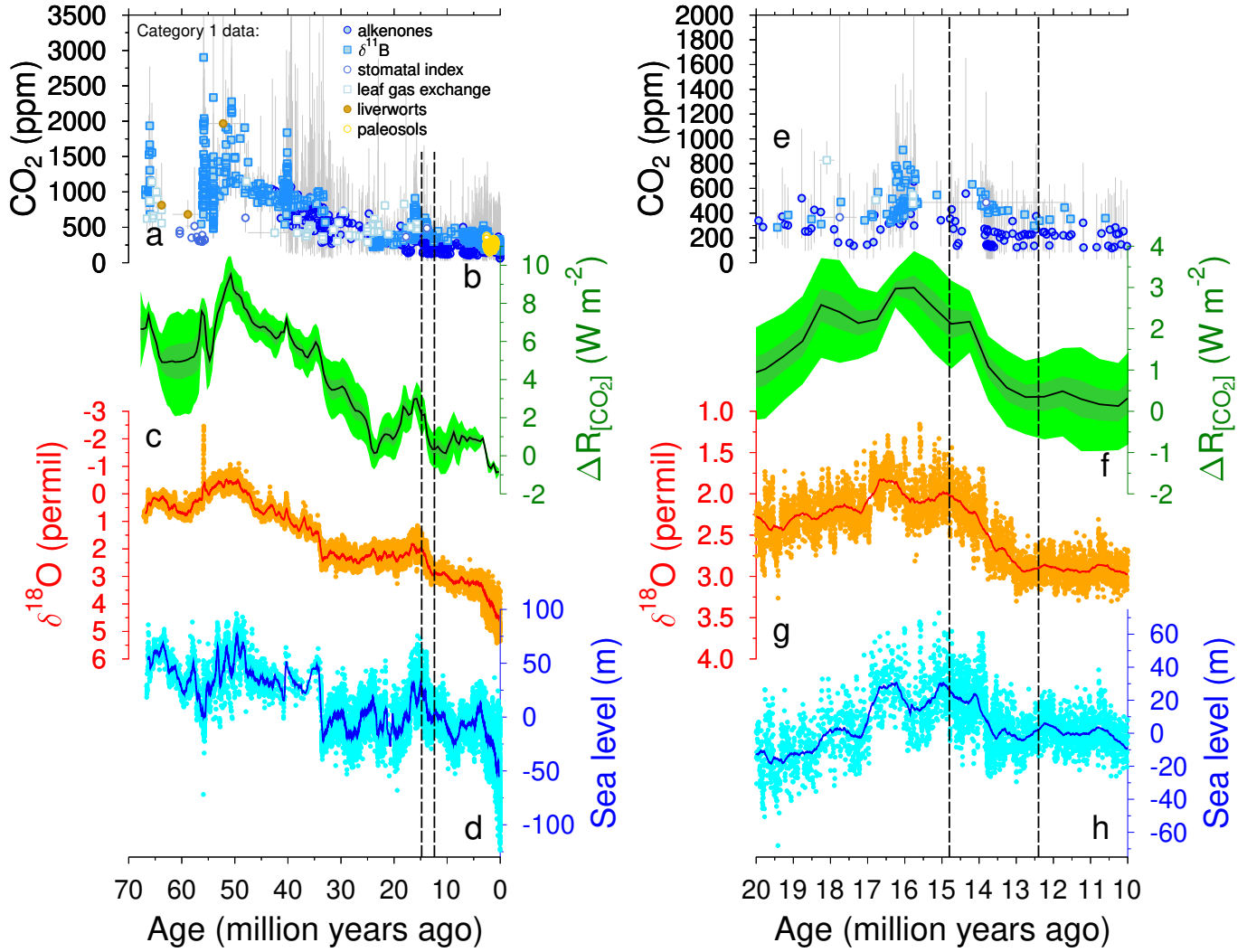

Fig. 4. Cenozoic climate change. (a) Most recent compilation of category 1 (most trustworthy) atmospheric CO_2 data (Cenozoic CO_2 Proxy Integration Project (CenCO_2PIP) Consortium 2023) as a function of proxy with their fully developed uncertainty estimates (95% confidence intervals). (b) CO_2 radiative forcing ($\Delta R_{[CO_2]} = 5.35[\ln(CO_2) - \ln(CO_{2,0})]$ W m^{-2}, $CO_{2,0} = 278$ ppm) of a 500-kyr running mean through data with median and 50 and 95% credible intervals: dark and light-green shading, respectively (Cenozoic CO_2 Proxy Integration Project (CenCO_2PIP) Consortium 2023). (c) benthic δ^{18}O recording a mixture of deep ocean temperature and sea level, raw data (points) and 500-kyr running mean (line) (Westerhold et al. 2020). (d) Reconstructed sea level change, raw data (points) and 500-kyr running mean (line) (Miller et al. 2020). Vertical broken lines mark the most likely time window (14.8–12.4 Myr ago, for $d_{\mathrm{Sun-cloud}}$ within 20–30 pc) of the Solar System being located in the dense region of the ISM suggested by this study. (e–h) Zoom in on the time window 20–10 Myr ago.

although the impact of dust on the climate is complex (Kok et al. 2023) and with significant uncertainties (Mahowald et al. 2023), it contributed to a radiative forcing of about -1 W m^{-2} (Köhler et al. 2010; Shaffer & Lambert 2018; Sherwood et al. 2020), roughly half of the change in radiative forcing caused by atmospheric CO_2. Given that the present-day global dust deposition rate on Earth is $5 \cdot 10^{15}$ g yr^{-1} (Kok et al. 2021), it would need to rise to $(2–4) \cdot 10^{16}$ g yr^{-1} in order achieve a radiative forcing similar to that proposed so far for CO_2 during the Middle Miocene climate transition. Furthermore, the current incoming flux of extraterrestrial dust load is $(1–2) \cdot 10^{10}$ g yr^{-1} on top of the atmosphere, which decreases to $(4–7) \cdot 10^{9}$ g yr^{-1} at the surface (Love & Brownlee 1993; Plane 2012; Rojas et al. 2021). Therefore, for the crossing of the Radcliffe wave to be the main driver of the Middle Miocene cooling, the extraterrestrial dust flux would need to rise by about 6–7 orders of magnitude to produce such a large anomaly in the radiation budget and the resulting climate effects. At present, the Sun is located at the edge of the Local Interstellar Cloud (LIC), a low-density cloudlet with $n_{\mathrm{H}} \sim 0.03–0.1$ cm^{-3} (see e.g., Gry & Jenkins 2014), located within a SN-generated hot void known as the Local Bubble, which has a characteristic density of $\sim$0.01 cm^{-3} (see e.g., Cox & Reynolds 1987; Linsky & Redfield 2021; Zucker et al. 2022; O'Neill et al. 2024). As the ISM density of the Radcliffe wave is significantly higher (ranging from 10^1 to 10^3 cm^{-3}) than the region currently traversed by the Solar System, the increase in the dust load on Earth could be at least of 2–5 orders of magnitude. Consequently, considering all factors and disregarding other differences in the climate system between the late Pleistocene and the Middle Miocene, our study suggests that the potential rise in extraterrestrial dust during the Solar System's crossing of the Radcliffe wave may have been 1–5 orders of magnitude smaller than necessary to fully account for the Middle Miocene climate transition as observed in the geological record.

At the moment, we can therefore infer that this process likely played a limited role in the Middle Miocene climate transition. However, once some of the underlying assumptions of this estimate are better constrained, the contribution to this event might be reassessed in either direction. Additionally, due to the non-permanent nature of any extraterrestrial dust influx associated with the Solar System's crossing, this process alone is unlikely to account for the long-term effect of a reduction in atmospheric CO_2. While it may have influenced climate during the multi-million years duration of the passage, other forcings or feedbacks would be required to explain the persistence of low temperatures and sea levels following the Middle Miocene climate transition.

To conclude, present day knowledge suggests that beyond small solar-driven climate oscillations (Eddy 1976), the long-term energy output of the Sun (Gough 1981) together with Earth's orbital parameters (Milankovic 1941), plate tectonics (Scotese 2021), deep carbon cycle (Müller et al. 2022), internal feedback (Ganopolski 2024), and very few large-scale meteorite impacts (Osinski et al. 2022; Zorzi et al. 2022) can explain a wide spectrum of the reconstructed changes and variability in Cenozoic climate. So far, all proposed additional extra-terrestrial influences have, to our knowledge, remained in a hypothetical state (Pavlov et al. 2005; Opher et al. 2024a) or even been discarded (Berger 1999; Carslaw et al. 2002; Bard & Frank 2006). However, we cannot rule out the possibility that an extraordinary amount of dust in the entire inner Solar System might have led to a reduction of incoming Solar radiation and a cooling on Earth, similar to what has been proposed for the triggering of the mid-Ordovician ice age 466 My ago (Schmitz et al. 2019). Furthermore, as shown by Miller et al. (2024), some effects of the Solar System's passage through a dense ISM region may be linked to nonpermanent, seasonal variations in cloud formation on Earth, which are more difficult to detect in paleo-records.

4.3. Caveats

Our results are based on the tracebacks of the orbits of the Solar System and of the clusters associated with the Radcliffe wave. As noted throughout the text, this method requires some approximations due to inherent difficulties in modeling the past structure and evolution of the gas. For example, we simplified the diverse and complex morphologies of the molecular clouds by assuming a spherical shape. Based on the principle of momentum conservation, we assumed that the motion of young clusters still reflects the movement of the gas nurseries from which they formed. We acknowledge that gravitational interactions and feedback from massive stars have likely influenced parts of the gas clouds and, consequently, the velocities of the clusters which formed within them. Thus, our tracebacks should be considered as a first approximation of the actual orbits. With these assumptions, we showed the general patterns of motion and estimate a time window during which the Solar System may have crossed the Radcliffe wave. Future studies will need to examine in greater detail the possible effects of gravity and feedback-induced displacements.

5. Conclusions

Our investigation reveals that the Solar System likely passed through the Orion region of the Radcliffe wave gas structure. By tracing back the orbits of the Sun and the Radcliffe wave's clusters, we constrain the time range of this crossing to be between 18.2 ± 0.1 and 11.5 ± 0.3 Myr ago, with the closest approaches ($d_{\mathrm{Sun-cloud}}$ within 20–30 pc) occurring within the interval of 14.8 ± 0.1 to 12.4 ± 0.2 Myr ago. As we do not account for potential gravitational interactions and feedback forces, we consider these time ranges to be preliminary approximations. Our results remain consistent even when varying solar parameters and Milky Way gravitational potentials.

The potentially increased amount of dust in the inner Solar System and in Earth's atmosphere resulting from such an interaction provides a framework for searching for isotopic anomalies in geological records older than 10 Myr. This is supported by our estimate that approximately 3^{+1}_{-2} SN occurred in the region traversed by the Sun, thus seeding it with freshly produced isotopes, such as ^{60}Fe. Additionally, we find that the period of closest approach was synchronous with the reorganization of the Earth's climate known as the Middle Miocene climate transition, even though a causal connection between the two events remains speculative and lacks direct evidence. In conclusion, our investigations underline the importance of studying the Galactic environment encountered by the Solar System during its orbit, along with the potential effects this may have on Earth.

Data availability

The supplementary figures of the Appendix are available online via Zenodo at the following link: https://doi.org/10.5281/zenodo.14626660. The code used for the analysis will be shared by EM upon reasonable request.
An animation associated to Fig. 3 is available at https://www.aanda.org

Acknowledgements. We thank the anonymous referee for the insightful comments, which have improved the quality and readability of the paper. JA and EM were co-funded by the European Union (ERC, ISM-FLOW, 101055318). S.R. acknowledges funding by the Austrian Research Promotion Agency (FFG, https://www.ffg.at/) under project number FO999892674. JG gratefully acknowledges co-funding from the European Union, the Central Bohemian Region, and the Czech Academy of Sciences, as part of the MERIT fellowship (MSCA-COFUND Horizon Europe, Grant Agreement No. 101081195). JG acknowledges the Collaborative Research Center 1601 (SFB 1601) funded by the Deutsche Forschungsgemeinschaft (DFG, German Research Foundation) – 500700252. This work has made use of data from the European Space Agency (ESA) mission *Gaia* https://www.cosmos.esa.int/gaia, processed by the *Gaia* Data Processing and Analysis Consortium (DPAC, https://www.cosmos.esa.int/web/gaia/dpac/consortium). Funding for the DPAC has been provided by national institutions, in particular the institutions participating in the *Gaia* Multilateral Agreement. This research has made use of publicly available software libraries, including galpy (Bovy 2015), Astropy (Astropy Collaboration 2022), NumPy (Harris et al. 2020), ALADIN (Bonnarel et al. 2000), TOPCAT (Taylor 2011), matplotlib (Hunter 2007), and plotly. The IMF has been sampled using the python code available at the following repository on github: https://github.com/keflavich/imf. The ages of the clusters have been estimated using the `Chronos` python code available at the following repository on github: https://github.com/ratzenboe/Chronos.

References

Abdurro'uf, Accetta, K., Aerts, C., et al. 2022, ApJS, 259, 35
Albani, S., Mahowald, N. M., Murphy, L. N., et al. 2016, Geophys. Res. Lett., 43, 3944
Almeida, A., Monteiro, H., & Dias, W. S. 2023, MNRAS, 525, 2315
Alonso-Santiago, J., Frasca, A., Bragaglia, A., et al. 2024, A&A, 691, A317
Altobelli, N., Kempf, S., Krüger, H., et al. 2005, J. Geophys. Res. (Space Phys.), 110, A07102
Alves, J., & Bouy, H. 2012, A&A, 547, A97
Alves, J., Zucker, C., Goodman, A. A., et al. 2020, Nature, 578, 237
André, P., Men'shchikov, A., Bontemps, S., et al. 2010, A&A, 518, L102
Arenou, F., Luri, X., Babusiaux, C., et al. 2018, A&A, 616, A17
Astropy Collaboration (Price-Whelan, A. M., et al.) 2022, ApJ, 935, 167

Ballesteros-Paredes, J., Román-Zúñiga, C., Salomé, Q., Zamora-Avilés, M., & Jiménez-Donaire, M. J. 2019, MNRAS, 490, 2648
Bally, J., Langer, W. D., Stark, A. A., & Wilson, R. W. 1987, ApJ, 312, L45
Bard, E., & Frank, M. 2006, Earth Planet. Sci. Lett., 248, 1
Barker, S., Lisiecki, L., Knorr, G., Nuber, S., & Tzedakis, P. 2025, Science, in press
Beaumont, C. N., Goodman, A. A., Alves, J. F., et al. 2012, MNRAS, 423, 2579
Bennett, M., & Bovy, J. 2019, MNRAS, 482, 1417
Berger, W. H. 1999, Int. J. Earth Sci., 88, 305
Bonnarel, F., Fernique, P., Bienaymé, O., et al. 2000, A&AS, 143, 33
Bovy, J. 2015, ApJS, 216, 29
Brandenburg, K. M., Rost, B., de Waal, D. B. V., Hoins, M., & Sluijs, A. 2022, Biogeosciences, 19, 3305
Breitschwerdt, D., Feige, J., Schulreich, M. M., et al. 2016, Nature, 532, 73
Bressan, A., Marigo, P., Girardi, L., et al. 2012, MNRAS, 427, 127
Briceno, C. 2008, in Handbook of Star Forming Regions, Volume I, 4, ed. B. Reipurth, 838
Brown, A. G. A., de Geus, E. J., & de Zeeuw, P. T. 1994, A&A, 289, 101
Buder, S., Sharma, S., Kos, J., et al. 2021, MNRAS, 506, 150
Cahlon, S., Zucker, C., Goodman, A., Lada, C., & Alves, J. 2024, ApJ, 961, 153
Cantat-Gaudin, T., Anders, F., Castro-Ginard, A., et al. 2020, A&A, 640, A1
Carslaw, K. S., Harrison, R. G., & Kirkby, J. 2002, Science, 298, 1732
Cenozoic CO_2 Proxy Integration Project ($CenCO_2PIP$) Consortium 2023, Science, 382, eadi5177
Chambers, K. C., Magnier, E. A., Metcalfe, N., et al. 2019, arXiv e-prints [arXiv:1612.05560]
Chen, B., Stoughton, C., Smith, J. A., et al. 2001, ApJ, 553, 184
Chen, B., D'Onghia, E., Alves, J., & Adamo, A. 2020a, A&A, 643, A114
Chen, B. Q., Li, G. X., Yuan, H. B., et al. 2020b, MNRAS, 493, 351
Chevance, M., Kruijssen, J. M. D., Vazquez-Semadeni, E., et al. 2020, Space Sci. Rev., 216, 50
Clark, P. U., Shakun, J. D., Rosenthal, Y., Köhler, P., & Bartlein, P. J. 2024, Science, 383, 884
Cox, D. P., & Reynolds, R. J. 1987, ARA&A, 25, 303
Dehnen, W., & Binney, J. J. 1998, MNRAS, 298, 387
Dharmawardena, T. E., Bailer-Jones, C. A. L., Fouesneau, M., et al. 2023, MNRAS, 519, 228
Eddy, J. A. 1976, Science, 192, 1189
Eisenhauer, F., Schödel, R., Genzel, R., et al. 2003, ApJ, 597, L121
Edenhofer, G., Zucker, C., Frank, P., et al. 2024, A&A, 685, A82
Fernández, D., Figueras, F., & Torra, J. 2008, A&A, 480, 735
Ferrière, K. M. 2001, Rev. Mod. Phys., 73, 1031
Fields, B. D., & Wallner, A. 2023, Annu. Rev. Nucl. Part. Sci., 73, 365
Flewelling, H. A., Magnier, E. A., Chambers, K. C., et al. 2020, ApJS, 251, 7
Foley, M. M., Goodman, A., Zucker, C., et al. 2023, ApJ, 947, 66
Francis, C., & Anderson, E. 2014, MNRAS, 441, 1105
Gaia Collaboration (Prusti, T., et al.) 2016, A&A, 595, A1
Gaia Collaboration (Brown, A. G. A., et al.) 2018, A&A, 616, A1
Gaia Collaboration (Vallenari, A., et al.) 2023, A&A, 674, A1
Ganopolski, A. 2024, Climate Past, 20, 151
Gillessen, S., Eisenhauer, F., Trippe, S., et al. 2009, ApJ, 692, 1075
Gontcharov, G. A. 2006, Astron. Astrophys. Trans., 25, 145
Gough, D. O. 1981, Sol. Phys., 74, 21
Gould, B. A. 1874, Am. J. Sci. Arts, 8, 325
Gowan, E. J., Zhang, X., Khosravi, S., et al. 2021, Nat. Commun., 12, 1199
GRAVITY Collaboration (Abuter, R., et al.) 2018, A&A, 615, L15
Green, G. M., Schlafly, E., Zucker, C., Speagle, J. S., & Finkbeiner, D. 2019, ApJ, 887, 93
Großschedl, J. E., Alves, J., Meingast, S., & Herbst-Kiss, G. 2021, A&A, 647, A91
Gry, C., & Jenkins, E. B. 2014, A&A, 567, A58
Hacar, A., Alves, J., Forbrich, J., et al. 2016, A&A, 589, A80
Hao, C. J., Xu, Y., Wu, Z. Y., et al. 2022, A&A, 660, A4
Harris, C. R., Millman, K. J., van der Walt, S. J., et al. 2020, Nature, 585, 357
He, Z., Wang, K., Luo, Y., et al. 2022, ApJS, 262, 7
Hennebelle, P., & Inutsuka, S.-i. 2019, Front. Astron. Space Sci., 6, 5
Hogg, D. W., Blanton, M. R., Roweis, S. T., & Johnston, K. V. 2005, ApJ, 629, 268
Hunt, E. L., & Reffert, S. 2023, A&A, 673, A114
Hunter, J. D. 2007, Comput. Sci. Eng., 9, 90
Imara, N., & Forbes, J. C. 2023, ApJ, 956, 114
Inutsuka, S.-i., Inoue, T., Iwasaki, K., & Hosokawa, T. 2015, A&A, 580, A49
Irrgang, A., Wilcox, B., Tucker, E., & Schiefelbein, L. 2013, A&A, 549, A137
Kamdar, H., Conroy, C., & Ting, Y.-S. 2021, arXiv e-prints [arXiv:2106.02050]
Kennicutt, R. C., & Evans, N. J. 2012, ARA&A, 50, 531
Kerr, F. J., & Lynden-Bell, D. 1986, MNRAS, 221, 1023
Knorr, G., & Lohmann, G. 2014, Nat. Geosci., 7, 376
Köhler, P., Bintanja, R., Fischer, H., et al. 2010, Q. Sci. Rev., 29, 129
Kok, J. F., Adebiyi, A. A., Albani, S., et al. 2021, Atmos. Chem. Phys., 21, 8127
Kok, J. F., Storelvmo, T., Karydis, V. A., et al. 2023, Nat. Rev. Earth Environ., 4, 71
Koll, D., Korschinek, G., Faestermann, T., et al. 2019, Phys. Rev. Lett., 123, 072701
Konietzka, R., Goodman, A. A., Zucker, C., et al. 2024, Nature, 628, 62
Kos, J., Bland-Hawthorn, J., Asplund, M., et al. 2019, A&A, 631, A166
Kounkel, M. 2020, ApJ, 902, 122
Krolikowski, D. M., Kraus, A. L., & Rizzuto, A. C. 2021, AJ, 162, 110
Kroupa, P. 2001, MNRAS, 322, 231
Lallement, R., Babusiaux, C., Vergely, J. L., et al. 2019, A&A, 625, A135
Lallement, R., Vergely, J. L., Babusiaux, C., & Cox, N. L. J. 2022, A&A, 661, A147
Larson, R. B. 1981, MNRAS, 194, 809
Laskar, J., Robutel, P., Joutel, F., et al. 2004, A&A, 428, 261
Leike, R. H., Glatzle, M., & Enßlin, T. A. 2020, A&A, 639, A138
Li, G.-X., Wyrowski, F., Menten, K., & Belloche, A. 2013, A&A, 559, A34
Linsky, J. L., & Redfield, S. 2021, ApJ, 920, 75
Liu, L., & Pang, X. 2019, ApJS, 245, 32
Love, S. G., & Brownlee, D. E. 1993, Science, 262, 550
Luo, A. L., Zhao, Y.-H., Zhao, G., et al. 2015, Res. Astron. Astrophys., 15, 1095
Mahowald, N. M., Li, L., Albani, S., Hamilton, D. S., & Kok, J. F. 2023, in AGU Fall Meeting Abstracts, 2023, A32C-01
Majewski, S. R., Schiavon, R. P., Frinchaboy, P. M., et al. 2017, AJ, 154, 94
McInnes, L., Healy, J., & Astels, S. 2017, J. Open Source Softw., 2, 205
McMillan, P. J. 2017, MNRAS, 465, 76
Meingast, S., Alves, J., & Rottensteiner, A. 2021, A&A, 645, A84
Milankovic, M. 1941, Kanon der Erdbestrahlung und seine Anwendung auf das Eiszeitenproblem, 1st edn. (Belgrade: Mihaila Curcica)
Miller, J. A., & Fields, B. D. 2022, ApJ, 934, 32
Miller, K. G., Browning, J. V., Schmelz, W. J., et al. 2020, Sci. Adv., 6, eaaz1346
Miller, J. A., Opher, M., Hatzaki, M., Papachristopoulou, K., & Thomas, B. C. 2024, Geophys. Res. Lett., 51, e2024GL110174
Miret-Roig, N., Galli, P. A. B., Brandner, W., et al. 2020, A&A, 642, A179
Molinari, S., Swinyard, B., Bally, J., et al. 2010, A&A, 518, L100
Motte, F., Bontemps, S., & Louvet, F. 2018, ARA&A, 56, 41
Müller, R. D., Mather, B., Dutkiewicz, A., et al. 2022, Nature, 605, 629
Nguyen, C. T., Costa, G., Girardi, L., et al. 2022, A&A, 665, A126
Nidever, D. L., Dey, A., Olsen, K., et al. 2018, AJ, 156, 131
O'Neill, T. J., Zucker, C., Goodman, A. A., & Edenhofer, G. 2024, ApJ, 973, 136
Opher, M., Loeb, A., & Peek, J. E. G. 2024a, Nat. Astron. 8, 983
Opher, M., Loeb, A., Zucker, C., et al. 2024b, ApJ, 972, 201
Osinski, G. R., Grieve, R. A., Ferrière, L., et al. 2022, Earth Sci. Rev., 232, 104112
Pavlidou, T., Scholz, A., & Teixeira, P. S. 2021, MNRAS, 503, 3232
Pavlov, A. A., Toon, O. B., Pavlov, A. K., Bally, J., & Pollard, D. 2005, Geophys. Res. Lett., 32, L03705
Phelps, S. R., Stoll, H. M., Bolton, C. T., Beaufort, L., & Polissar, P. J. 2021, Geochem. Geophys. Geosyst., 22, e2021GC009658
Plane, J. M. C. 2012, Chem. Soc. Rev., 41, 6507
Posch, L., Miret-Roig, N., Alves, J., et al. 2023, A&A, 679, L10
Rae, J. W. B., Zhang, Y. G., Liu, X., et al. 2021, Annu. Rev. Earth Planet. Sci., 49
Randich, S., Gilmore, G., Magrini, L., et al. 2022, A&A, 666, A121
Ratzenböck, S., Großschedl, J. E., Möller, T., et al. 2023a, A&A, 677, A59
Ratzenböck, S., Großschedl, J. E., Alves, J., et al. 2023b, A&A, 678, A71
Rea, D. K. 1994, Rev. Geophys., 32, 159
Rohling, E. J., Gernon, T. M., Heslop, D., et al. 2024, Paleoceanogr. Paleoclimatol., 39, e2024PA004872
Rojas, J., Duprat, J., Engrand, C., et al. 2021, Earth Planet Sci. Lett., 560, 116794
Schmitz, B., Farley, K. A., Goderis, S., et al. 2019, Sci. Adv., 5, eaax4184
Schönrich, R., Binney, J., & Dehnen, W. 2010, MNRAS, 403, 1829
Schulreich, M. M., Breitschwerdt, D., Feige, J., & Dettbarn, C. 2017, A&A, 604, A81
Schulreich, M. M., Feige, J., & Breitschwerdt, D. 2023, A&A, 680, A39
Scotese, C. R. 2021, Annu. Rev. Earth Planet. Sci., 49
Shaffer, G., & Lambert, F. 2018, PNAS, 115, 2026
Shapley, H. 1921, J. Geol., 29, 502
Sherwood, S. C., Webb, M. J., Annan, J. D., et al. 2020, Rev. Geophys., 58, e2019RG000678
Shetty, R., Collins, D. C., Kauffmann, J., et al. 2010, ApJ, 712, 1049
Sim, G., Lee, S. H., Ann, H. B., & Kim, S. 2019, J. Korean Astron. Soc., 52, 145
Skrutskie, M. F., Cutri, R. M., Stiening, R., et al. 2006, AJ, 131, 1163
Snow, T. P., & McCall, B. J. 2006, ARA&A, 44, 367
Stap, L. B., Berends, C. J., & van de Wal, R. S. W. 2024, Climate Past, 20, 257
Steinmetz, M., Matijevič, G., Enke, H., et al. 2020, AJ, 160, 82

Steinthorsdottir, M., Coxall, H. K., de Boer, A. M., et al. 2021, Paleoceanogr. Paleoclimatol., 36, e2020PA004037
Swiggum, C., Alves, J., D'Onghia, E., et al. 2022, A&A, 664, L13
Swiggum, C., Alves, J., Benjamin, R., et al. 2024, Nature, 631, 49
Szilágyi, M., Kun, M., & Ábrahám, P. 2021, MNRAS, 505, 5164
Talbot, R. J., & Newman, M. J. 1977, ApJS, 34, 295
Taylor, M. 2011, TOPCAT: Tool for OPerations on Catalogues And Tables, Astrophysics Source Code Library [record ascl:1101.010]
Tierney, J. E., Zhu, J., King, J., et al. 2020, Nature, 584, 569
Tobin, J. J., Hartmann, L., Furesz, G., Mateo, M., & Megeath, S. T. 2009, ApJ, 697, 1103
Torres, C. A. O., Quast, G. R., da Silva, L., et al. 2006, A&A, 460, 695
Tsantaki, M., Pancino, E., Marrese, P., et al. 2022, A&A, 659, A95
van de Wal, R. S. W., de Boer, B., Lourens, L. J., Köhler, P., & Bintanja, R. 2011, Climate Past, 7, 1459
Vanhollebeke, E., Groenewegen, M. A. T., & Girardi, L. 2009, A&A, 498, 95
Vergely, J. L., Lallement, R., & Cox, N. L. J. 2022, A&A, 664, A174
Walch, S., & Naab, T. 2015, MNRAS, 451, 2757
Wallner, A., Faestermann, T., Feige, J., et al. 2015, Nat. Commun., 6, 5956
Wallner, A., Froehlich, M. B., Hotchkis, M. A. C., et al. 2021, Science, 372, 742
Westerhold, T., Marwan, N., Drury, A. J., et al. 2020, Science, 369, 1383
Zhao, G., Zhao, Y.-H., Chu, Y.-Q., Jing, Y.-P., & Deng, L.-C. 2012, Res. Astron. Astrophys., 12, 723
Zorzi, A., Tikoo, S. M., Beroza, G. C., & Sleep, N. H. 2022, Geophys. Res. Lett., 49, e99313
Zucker, C., Battersby, C., & Goodman, A. 2018, ApJ, 864, 153
Zucker, C., Speagle, J. S., Schlafly, E. F., et al. 2019, ApJ, 879, 125
Zucker, C., Goodman, A. A., Alves, J., et al. 2022, Nature, 601, 334

Appendix A: Properties of the clusters

In this appendix, we provide supplementary plots and a comparison with the literature for the ages and masses of the Radcliffe wave's clusters used in this study. In Table A.1, the initial positions and velocities of these clusters, along with the errors, are listed. Additionally, we describe our method for estimating the number of past supernova (SN) events.

A.1. Age computation

In Sect. 3.2, we outline the method used to compute the ages of the clusters. The color-magnitude diagrams for the 56 clusters of the Radcliffe wave used in this study are shown in Fig. A.1 and A.2. The estimated ages are listed in Table A.2.

In Fig. A.3, we present the comparison between the ages of the clusters computed with `Chronos` (Ratzenböck et al. 2023b) and those provided by the source catalogs. It is possible to note that, in general, the estimated ages are consistent with each other. Exceptions are observed for certain clusters, namely CWNU 1088 ($\mathrm{age}_{\mathrm{Chronos}} = 1.7^{+1.4}_{-0.1}$ Myr; $\mathrm{age}_{\mathrm{catalog}} = 30^{+34}_{-19}$ Myr), L1524 ($\mathrm{age}_{\mathrm{Chronos}} = 8.5^{+2.7}_{-3.4}$ Myr; $\mathrm{age}_{\mathrm{catalog}} = 187^{+808}_{-137}$ Myr), L1546 ($\mathrm{age}_{\mathrm{Chronos}} = 1.9^{+1.1}_{-0.3}$ Myr; $\mathrm{age}_{\mathrm{catalog}} = 15^{+22}_{-11}$ Myr), and NGC 1977 ($\mathrm{age}_{\mathrm{Chronos}} = 6.8^{+1.6}_{-1.1}$ Myr; $\mathrm{age}_{\mathrm{catalog}} = 97.7$ Myr–error not provided) for which the ages calculated with `Chronos` are notably younger. In addition, given the estimated age uncertainty, the `Chronos`' ages are likely more precise when compared to the ones given in the cluster catalog. Moreover, some of the selected clusters have already been studied in other literature, and their computed ages are consistent with our results. For instance, the ages of OBP-West (also known as ASCC 18), ASCC 20, and ASCC 21 have been estimated (Kos et al. 2019) to be about 12.75 ± 1.27 Myr, 21.25 ± 2.12 Myr, and 11.0 ± 1.1 Myr respectively. In our analysis, these clusters are $12.8^{+1.4}_{-1.7}$, $19.3^{+6.6}_{-0.2}$, and $12.6^{+0.2}_{-1.8}$ Myr old. The age of NGC 1980 has been computed (Alves & Bouy 2012) to be between 5 and 10 Myr, in agreement with our range of 7.3 and 8.5 Myr.

A.2. Mass computation

The masses of the clusters are estimated as described in Sect. 3.2 and reported in Table A.2. In Fig. A.4, we show the best-fit mass functions, together with the observed ones, for each of the analyzed clusters. The plots show that all the populations exhibit a truncation at the low-mass end caused by sensitivity limits. We also observe that the mass distributions are adequately sampled up to several Solar masses for some clusters, whereas for others, they are truncated (e.g., HSC 1640). This truncation may be attributed to catalog incompleteness (too bright sources) or stellar evolution processes (SN in the past).

By comparing the masses of our clusters with those found in the literature (see e.g., Alves & Bouy 2012; Almeida et al. 2023), we confirm that our values are generally lower estimates, as HR23 prioritized precision over completeness, aiming to minimize the number of false positives associated with each cluster. For example, the mass of Briceno 1 (also known as ASCC 16) has been estimated to have about $441 \pm 88\,M_\odot$ (Almeida et al. 2023), more than double our own estimation of $205\,M_\odot$. The same happens for NGC 1980, for which a mass of $1000\,M_\odot$ has been computed (Alves & Bouy 2012), twice as much than what we obtain. Instead, for OBP-d (also known as Theia-13) the estimated mass of $365 \pm 73\,M_\odot$ (Almeida et al. 2023), aligns closely with our estimate of $340\,M_\odot$.

A.3. Estimation of the past supernova events

To determine whether radionuclides were present during the encounter of the Sun with the Radcliffe wave, we estimate the number of possible SN that occurred in the region of interest before 11.5 ± 0.3 Myr ago. This time threshold is chosen because it corresponds to the estimated period when the crossing of the Radcliffe wave likely ended (assuming cloud radii of 50 pc). We focused on 37 out of the 56 clusters, which are the ones that are currently located in the Orion star-forming region, as this is the region to which the Sun gets closer.

For a given cluster, we used the estimated mass corrected for incompleteness (see Sect. 3.2) and Kroupa IMF (Kroupa 2001), to generate its stellar content. We then counted the number of stars with a mass greater than the highest one predicted by a stellar isochrone model (Bressan et al. 2012; Nguyen et al. 2022) corresponding to an age equal to that of the analyzed cluster 11.5 Myr ago. Clusters that are younger than 11.5 Myr were not considered. In this way, we were able to roughly estimate the number of massive stars that had time to evolve and, eventually, explode as a SN. We repeated this process multiple times in order to account for errors in the clusters' ages, the timing of the Sun exiting the Radcliffe wave, and the variability in the number of stars produced by the IMF. We estimate that approximately 3^{+1}_{-2} SN occurred before 11.5 Myr ago, suggesting that the Sun passed through freshly enriched clouds. This value, in line with studies on SN in young clusters (Foley et al. 2023), is likely underestimated due to catalog incompleteness, which consequently affects the mass estimates of the clusters. If we hypothesize that half of the actual clusters mass is missing from our estimates, as found in some cases, the number of SN would be 8^{+1}_{-4}.

Appendix B: Initial condition tests

In this appendix, we present how different initial conditions influence our results. In particular, we used different solar parameters and various Milky Way potentials from the literature. We performed multiple sets of orbit integrations using the procedure described in Sect. 3.4, varying a parameter or a combination of parameters in each run, to evaluate how the crossing times of the Solar System with the Radcliffe wave are influenced by them.

In our main study, we used `galpy`'s `MWPotential2014` as a model for the Milky Way potential. This model includes a bulge, a disk, and a halo component (Bovy 2015). We assumed the distance of the Sun from the Galactic center to be $R_\odot = 8.33$ kpc (Gillessen et al. 2009), its vertical position respect to the disk to be $z_\odot = 27$ pc (Chen et al. 2001), and its velocity relative to the Local Standard of Rest ($v_{\mathrm{LSR}} = 220\,\mathrm{km\,s^{-1}}$) to be $(U_\odot, V_\odot, W_\odot) = (11.1, 12.24, 7.25)\,\mathrm{km\,s^{-1}}$ (Schönrich et al. 2010).

In an alternative set-up, we examined the scenario where the Sun's Galactocentric distance and height above the plane are set to $R_\odot = 8.122$ kpc (GRAVITY Collaboration 2018) and $z_\odot = 20.8$ pc (Bennett & Bovy 2019), respectively. Moreover, we explored two other models of the Milky Way's potential included in `galpy`. In one model (McMillan 2017), the Local Standard of Rest has a circular velocity of $233\,\mathrm{km\,s^{-1}}$ and the Galactocentric radius is $R_\odot = 8.2$ kpc; while in the second model (Irrgang et al. 2013), the Local Standard of Rest has a circular velocity of $242\,\mathrm{km\,s^{-1}}$, with $R_\odot = 8.4$ kpc. Moreover, we investigated the effect that different peculiar velocities of the Sun would have on our results, using $(U_\odot, V_\odot, W_\odot) = (10.1, 4.0, 6.7)\,\mathrm{km\,s^{-1}}$ (Hogg et al. 2005), $(10.0, 5.25, 7.17)\,\mathrm{km\,s^{-1}}$ (Dehnen & Binney 1998), or $(10.0, 15.4, 7.8)\,\mathrm{km\,s^{-1}}$ (Kerr & Lynden-Bell 1986). The full list of cases analyzed, along with the computed transit times between

Table A.1: Cartesian coordinates (X, Y, Z) and velocities (U, V, W) with respect to the Sun, together with the corresponding errors, for the 56 identified clusters of the Radcliffe wave within the region of interest for this study.

Name in catalog	X [pc]	Y [pc]	Z [pc]	U [km s^{-1}]	V [km s^{-1}]	W [km s^{-1}]	$X_{\rm err}$ [pc]	$Y_{\rm err}$ [pc]	$Z_{\rm err}$ [pc]	$U_{\rm err}$ [km s^{-1}]	$V_{\rm err}$ [km s^{-1}]	$W_{\rm err}$ [km s^{-1}]
Briceno 1	-302.44	-116.94	-107.91	-18.19	-8.26	-4.60	0.49	0.20	0.20	0.21	0.08	0.08
ASCC 18	-359.37	-147.74	-130.29	-25.13	-8.07	-7.05	2.21	1.03	0.93	0.49	0.27	0.21
Theia 13	-351.87	-165.40	-127.41	-25.92	-12.70	-9.39	0.77	0.39	0.31	0.39	0.17	0.16
Sigma Orionis	-336.25	-169.96	-116.64	-25.54	-15.57	-6.86	0.57	0.32	0.25	0.18	0.14	0.12
NGC 1980	-309.96	-175.65	-127.38	-22.22	-12.84	-6.59	0.50	0.27	0.20	0.16	0.09	0.07
UBC 207	-319.00	-171.44	-124.37	-24.13	-12.60	-7.13	1.11	0.57	0.40	0.33	0.20	0.14
NGC 1977	-321.63	-174.10	-127.01	-24.49	-15.65	-8.40	0.70	0.38	0.29	0.43	0.24	0.20
ASCC 19	-301.08	-139.19	-116.56	-18.49	-11.54	-6.62	0.50	0.34	0.31	0.79	0.37	0.32
ASCC 20	-318.64	-126.23	-109.39	-27.19	-8.93	-9.29	1.02	0.39	0.33	0.31	0.13	0.11
ASCC 21	-305.74	-111.92	-96.40	-17.52	-8.76	-3.63	0.37	0.37	0.18	0.66	0.24	0.21
Alessi-Teutsch 10	-351.13	111.51	-129.20	-20.21	-4.87	-9.93	1.91	0.64	0.88	1.58	0.57	0.52
CWNU 1028	-265.22	-132.82	-143.96	-15.76	-10.10	-7.87	1.61	1.22	0.83	0.40	0.33	0.35
CWNU 1072	-362.98	-215.24	-121.07	-24.92	-11.66	-12.68	2.94	1.93	0.98	0.99	0.63	0.36
CWNU 1088	-384.68	-190.09	-117.90	-13.10	-16.78	-6.28	16.94	7.52	4.82	2.18	1.48	0.73
CWNU 1092	-380.77	-139.44	-47.32	-23.97	-13.06	-12.87	2.13	0.99	0.69	0.75	0.10	0.14
CWNU 1106	-374.42	-125.68	-66.33	-24.90	-10.93	-13.93	2.26	0.82	0.58	0.01	0.17	0.24
CWNU 1129	-150.26	15.18	-43.44	-17.07	-13.10	-6.93	0.61	1.23	0.34	0.25	0.11	0.10
Collinder 69	-370.78	-101.25	-81.02	-24.46	-11.19	-5.60	0.48	0.29	0.19	0.15	0.10	0.06
HSC 1250	-252.15	97.91	-100.59	-16.80	-9.42	-7.20	1.01	0.91	0.99	0.66	0.40	0.39
HSC 1262	-348.18	128.73	-96.31	-23.82	-2.09	-7.16	0.92	0.45	0.36	0.68	0.31	0.22
HSC 1318	-122.48	23.79	-34.52	-16.45	-11.98	-10.88	0.34	0.31	0.23	0.28	0.13	0.10
HSC 1340	-112.14	5.26	-39.44	-13.82	-6.32	-9.99	0.56	0.83	0.50	0.52	0.08	0.19
HSC 1373	-107.86	29.33	-82.42	-12.43	-5.41	-5.95	1.43	2.48	0.81	0.91	0.29	0.99
HSC 1481	-203.09	-10.93	-46.30	-16.40	-8.05	-8.83	1.56	2.51	0.77	1.54	0.21	0.09
HSC 1633	-310.87	-155.53	-136.51	-17.98	-12.91	-5.71	0.93	0.55	0.48	1.10	0.44	0.36
HSC 1640	-170.63	-85.40	-135.32	-6.83	-8.63	-6.01	2.30	1.40	1.16	0.88	0.36	0.56
HSC 1648	-228.05	-120.40	-117.82	-10.75	-11.54	-7.14	1.40	0.51	0.53	1.19	0.67	0.65
HSC 1653	-242.87	-138.68	-126.54	-12.48	-7.97	-6.28	0.96	0.57	0.54	1.50	0.86	0.72
HSC 1692	-197.27	-137.93	-101.25	-22.99	-5.87	-6.85	3.75	2.58	1.65	0.65	0.30	0.48
IC 348	-279.68	99.15	-95.34	-16.38	-5.93	-7.42	4.47	1.56	1.56	0.14	0.08	0.07
L 1641S	-333.57	-212.08	-135.95	-16.74	-11.52	-7.12	1.92	1.20	0.81	0.44	0.27	0.19
Mamajek 3	-91.23	-26.63	-27.52	-11.04	-19.01	-8.52	0.89	0.55	0.40	0.82	0.29	0.25
NGC 1333	-253.54	100.43	-101.39	-16.39	-10.66	-9.52	0.86	0.38	0.38	0.62	0.31	0.27
NGC 2068	-355.29	-166.57	-100.86	-23.81	-11.87	-8.68	0.89	0.50	0.30	0.28	0.17	0.17
OC 0340	-352.44	-160.61	-113.16	-24.00	-11.95	-9.57	3.31	1.54	1.09	1.96	0.74	0.50
OCSN 50	-175.67	22.91	-71.36	-14.35	-5.76	-5.32	2.04	1.63	0.53	0.96	0.16	0.43
OCSN 56	-371.51	-138.14	-108.89	-28.20	-8.28	-9.37	1.16	0.80	0.67	1.00	0.36	0.39
OCSN 59	-318.14	-138.39	-155.33	-18.37	-10.62	-7.70	0.62	0.40	0.57	1.19	0.63	0.50
OCSN 61	-331.92	-152.78	-110.51	-26.86	-12.36	-11.18	0.81	0.45	0.41	0.83	0.39	0.29
OCSN 64	-268.51	-132.13	-122.54	-26.17	-5.31	-5.58	14.02	6.97	6.04	1.31	0.78	0.68
OCSN 65	-356.47	-170.22	-125.64	-25.48	-9.35	-9.48	1.23	0.67	0.52	1.08	0.48	0.46
OCSN 68	-345.31	-194.74	-135.39	-25.48	-9.74	-11.14	1.52	1.55	0.80	0.84	0.48	0.35
OCSN 70	-334.34	-221.18	-144.60	-14.34	-12.41	-6.35	0.78	0.60	0.48	0.44	0.28	0.30
OC 0279	-255.68	84.10	-80.35	-18.21	-9.86	-8.76	1.02	0.50	0.54	0.53	0.20	0.16
OC 0280	-337.87	101.55	-95.04	-20.82	-5.01	-7.35	1.30	0.46	0.77	1.17	0.34	0.35
OC 0339	-310.52	-139.57	-108.15	-18.43	-11.20	-5.15	0.52	0.43	0.45	0.26	0.12	0.08
OC 0356	-344.73	-230.65	-149.48	-13.86	-13.13	-6.99	0.85	0.67	0.45	0.82	0.27	0.12
Theia 54	-153.64	17.76	-21.40	-15.87	-14.82	-10.38	0.72	0.51	0.76	0.76	0.15	0.12
Theia 65	-107.30	-6.84	-9.24	-12.61	-18.73	-8.63	0.52	0.74	0.66	0.75	0.13	0.11
Theia 66	-135.79	1.51	-48.71	-16.81	-15.20	-7.59	0.45	0.47	0.33	0.36	0.12	0.14
Theia 7	-122.75	12.78	-34.07	-16.02	-11.06	-9.48	0.69	0.43	0.25	0.26	0.11	0.14
Theia 93	-172.95	-3.23	-19.75	-17.47	-13.49	-9.22	1.01	0.70	0.65	1.08	0.31	0.21
UBC 17a	-306.62	-150.75	-103.93	-17.99	-12.63	-4.93	0.57	0.53	0.39	0.37	0.24	0.14
UPK 398	-403.81	-137.17	-86.49	-27.14	-9.67	-13.53	1.43	0.60	0.33	1.90	0.65	0.48
UPK 402	-356.17	-153.64	-84.64	-20.06	-11.08	-8.23	1.49	0.67	0.41	1.06	0.41	0.30
UPK 422	-234.56	-154.66	-86.42	-12.13	-8.87	-4.82	0.96	0.51	0.39	0.49	0.33	0.21

Notes. The first seven clusters are those with which the Sun's orbits get closer than 50 pc during their cloud phase, as identified in this study (see Table 1).

the Sun and the Radcliffe wave for various threshold distances ($d_{\rm Sun-cloud}$), is provided in Table B.1. From these tests, we conclude that over the 30 Myr integration period, our results are robust and do not vary significantly when considering different initial conditions.

Table A.2: Properties of the 56 Radcliffe wave's clusters selected for this study.

Name in this work	Name in catalog	Region	N_c	$Age_{Chronos}$	M^{cls}	M^{cls}_*	$M^{cloud}_{SFE=1\%}$	$R_{SFE=1\%}$	$M^{cloud}_{SFE=3\%}$	$R_{SFE=3\%}$
				(Myr)	[$M_\odot$]	[$M_\odot$]	[$M_\odot$]	[pc]	[$M_\odot$]	[pc]
Briceno 1	Briceno 1	Orion	171	$12.7^{+1.5}_{-0.1}$	107	205	20500	15.7	6833	10.7
OBP-West	ASCC 18	Orion	82	$12.8^{+1.4}_{-1.7}$	64	155	15500	14.2	5167	9.7
OBP-d	Theia 13	Orion	249	$10.3^{+1.0}_{-1.1}$	156	340	34000	18.7	11333	12.8
Sigma Orionis	Sigma Orionis	Orion	181	$3.4^{+0.7}_{-0.5}$	120	188	18750	15.2	6250	10.4
NGC 1980	NGC 1980	Orion	364	$8.1^{+0.4}_{-0.8}$	226	490	49000	21.2	16333	14.5
NGC 1981	UBC 207	Orion	53	$6.0^{+1.5}_{-0.7}$	34	92	9250	11.9	3083	8.2
NGC 1977	NGC 1977	Orion	111	$6.8^{+1.6}_{-1.1}$	92	255	25500	16.9	8500	11.6
OBP-Near-1	ASCC 19	Orion	61	$12.5^{+0.4}_{-1.5}$	51	115	11500	12.8	3833	8.8
ASCC 20	ASCC 20	Orion	194	$19.3^{+6.6}_{-0.2}$	138	255	25500	16.9	8500	11.6
ASCC 21	ASCC 21	Orion	116	$12.6^{+0.2}_{-1.8}$	102	198	19750	15.5	6583	10.6
Heleus	Alessi-Teutsch 10	Perseus	85	$6.4^{+1.1}_{-0.8}$	52	82	8250	11.5	2750	7.8
IC2118-Halo	CWNU 1028	Orion	19	$13.4^{+3.7}_{-3.2}$	15	30	3000	8.1	1000	5.5
Orion-A-East	CWNU 1072	Orion	60	$20.5^{+1.2}_{-3.3}$	34	85	8500	11.6	2833	7.9
L1630-background	CWNU 1088	Orion	46	$1.7^{+1.4}_{-0.1}$	17	28	2750	7.8	917	5.4
L1598-East	CWNU 1092	Orion	27	$25.0^{+18.2}_{-0.6}$	24	48	4750	9.5	1583	6.5
L1598	CWNU 1106	Orion	16	$5.5^{+0.8}_{-0.9}$	10	25	2500	7.6	833	5.2
L1546	CWNU 1129	Taurus	34	$1.9^{+1.2}_{-0.3}$	7	8	750	5.0	250	3.4
lambda-Ori	Collinder 69	Orion	1247	$7.2^{+0.7}_{-0.2}$	741	1442	144250	30.7	48083	21.0
Autochthe-Gorgophone	HSC 1250	Perseus	34	$6.8^{+3.9}_{-1.4}$	27	55	5500	10.0	1833	6.8
Mestor	HSC 1262	Perseus	143	$8.4^{+0.7}_{-2.2}$	81	150	15000	14.1	5000	9.6
L1495	HSC 1318	Taurus	52	$4.7^{+1.6}_{-1.5}$	24	40	4000	8.9	1333	6.1
HSC 1340	HSC 1340	Taurus	194	$27.2^{+4.1}_{-2.3}$	98	220	22000	16.1	7333	11.0
HSC 1373	HSC 1373	Taurus	46	$21.3^{+8.9}_{-2.5}$	20	40	4000	8.9	1333	6.1
HSC 1481	HSC 1481	Taurus	40	$22.4^{+15.5}_{-3.4}$	15	28	2750	7.8	917	5.4
L1634-North	HSC 1633	Orion	68	$9.2^{+0.6}_{-2.9}$	42	98	9750	12.1	3250	8.3
Eridanus-North	HSC 1640	Orion	128	$15.5^{+2.6}_{-0.7}$	64	145	14500	13.9	4833	9.5
Rigel	HSC 1648	Orion	78	$13.0^{+0.8}_{-1.6}$	39	65	6500	10.6	2167	7.2
L1634-South	HSC 1653	Orion	30	$10.0^{+9.6}_{-1.6}$	16	32	3250	8.3	1083	5.7
HSC 1692	HSC 1692	Orion	24	$27.7^{+5.4}_{-1.9}$	13	30	3000	8.1	1000	5.5
IC 348	IC 348	Perseus	302	$4.9^{+1.2}_{-2.2}$	151	295	29500	17.8	9833	12.2
L1641-South	L 1641S	Orion	72	$9.0^{+2.0}_{-2.6}$	53	155	15500	14.2	5167	9.7
Mamajek 3	Mamajek 3	Taurus	33	$17.6^{+9.6}_{-0.8}$	19	42	4250	9.1	1417	6.2
NGC 1333	NGC 1333	Perseus	31	$3.8^{+1.9}_{-0.9}$	10	10	1000	5.5	333	3.8
NGC 2068	NGC 2068	Orion	102	$3.3^{+0.7}_{-0.8}$	65	142	14250	13.8	4750	9.5
OC 0340	OC 0340	Orion	17	$13.4^{+3.3}_{-4.9}$	30	20	2000	7.0	667	4.8
OCSN 50	OCSN 50	Taurus	24	$18.1^{+8.1}_{-5.2}$	13	30	3000	8.1	1000	5.5
omega-Ori	OCSN 56	Orion	88	$17.7^{+2.5}_{-1.8}$	57	130	13000	13.4	4333	9.2
L1616	OCSN 59	Orion	60	$8.3^{+2.0}_{-0.9}$	36	75	7500	11.1	2500	7.6
OBP-b	OCSN 61	Orion	147	$19.6^{+0.3}_{-1.4}$	94	170	17000	14.7	5667	10.1
OBP-e	OCSN 64	Orion	67	$18.2^{+6.9}_{-2.3}$	45	82	8250	11.5	2750	7.8
OBP-far	OCSN 65	Orion	70	$17.1^{+3.4}_{-2.4}$	43	95	9500	12.0	3167	8.2
OCSN 68	OCSN 68	Orion	51	$20.5^{+1.7}_{-5.5}$	29	68	6750	10.7	2250	7.3
L1647-North	OCSN 70	Orion	18	$9.9^{+7.2}_{-6.4}$	15	38	3750	8.7	1250	6.0
Alcaeus	OC 0279	Perseus	146	$13.4^{+5.6}_{-1.3}$	82	145	14500	13.9	4833	9.5
Electryon-Cynurus	OC 0280	Perseus	78	$13.5^{+3.0}_{-5.1}$	58	152	15250	14.2	5083	9.7
OBP-Near-3	OC 0339	Orion	19	$12.9^{+11.0}_{-5.5}$	10	20	2000	7.0	667	4.8
L1647-Main	OC 0356	Orion	15	$5.7^{+2.3}_{-2.2}$	9	25	2500	7.6	833	5.2
L1517	Theia 54	Taurus	48	$7.7^{+2.0}_{-2.8}$	33	52	5250	9.8	1750	6.7
118Tau	Theia 65	Taurus	37	$14.1^{+2.7}_{-2.1}$	17	32	3250	8.3	1083	5.7
L1551	Theia 66	Taurus	39	$5.1^{+2.4}_{-1.3}$	19	30	3000	8.1	1000	5.5
L1524	Theia 7	Taurus	47	$8.5^{+2.7}_{-3.4}$	26	65	6500	10.6	2167	7.2
L1544	Theia 93	Taurus	91	$10.7^{+2.0}_{-1.9}$	49	128	12750	13.3	4250	9.1
OBP-Near-2	UBC 17a	Orion	102	$6.3^{+0.5}_{-0.5}$	70	118	11750	12.9	3917	8.9
lambda-Ori-South	UPK 398	Orion	84	$10.1^{+4.1}_{-1.1}$	45	95	9500	12.0	3167	8.2
L1617	UPK 402	Orion	47	$5.9^{+1.3}_{-1.8}$	27	62	6250	10.4	2083	7.1
Orion-Y	UPK 422	Orion	240	$25.1^{+0.6}_{-6.3}$	140	300	30000	17.9	10000	12.2

Notes. For each cluster, the following information is provided: the name used in this work and the one from the source catalogs (Hunt & Reffert 2023; Cantat-Gaudin et al. 2020; Sim et al. 2019; Hao et al. 2022; He et al. 2022; Szilágyi et al. 2021; Liu & Pang 2019), the region to which they are associated, the number of stellar members (N_c), the estimated isochronal age ($Age_{Chronos}$), the cluster's mass derived from the stellar members (M^{cls}), and corrected for incompleteness (M^{cls}_*). Additionally, the mass and radius of the cloud associated with the cluster are given assuming a SFE of 1% and 3% ($M^{cloud}_{SFE=1(3)\%}$, $R_{SFE=1(3)\%}$).

Table B.1: Test of initial conditions to assess the robustness of our findings.

Parameter Investigated	Potential	$d_\odot$	$z_\odot$	$(U_\odot, V_\odot, W_\odot)$	Ref.	$d_{\mathrm{Sun-cloud}} \leq 50$ pc	$d_{\mathrm{Sun-cloud}} \leq 40$ pc	$d_{\mathrm{Sun-cloud}} \leq 30$ pc	$d_{\mathrm{Sun-cloud}} \leq 20$ pc
		[kpc]	[pc]	[km s^{-1}]		(t_{enter}, t_{exit}) (Myr)	(t_{enter}, t_{exit}) (Myr)	(t_{enter}, t_{exit}) (Myr)	(t_{enter}, t_{exit}) (Myr)
Ref.Case	mwp14*	8.3	27	(11.1, 12.24, 7.25)	a_1,b_1,c_1,d_1	$(-18.2 \pm 0.1, -11.5 \pm 0.3)$	$(-17.4 \pm 0.2, -11.9 \pm 0.3)$	$(-14.8 \pm 0.1, -12.4 \pm 0.2)$	$(-14.3 \pm 0.1, -12.8 \pm 0.2)$
Sun Galactocentric dist.	mwp14	7.5	27	(11.1, 12.24, 7.25)	a_1,b_2,c_1,d_1	$(-18.0 \pm 0.1, -11.5 \pm 0.6)$	$(-15.2 \pm 0.2, -12.1 \pm 0.3)$	$(-14.6 \pm 0.2, -12.6 \pm 0.2)$	$(-14.5 \pm 0.2, -12.6 \pm 0.3)_{d\leq 27.5\,\mathrm{pc}}$
	mwp14	7.94	27	(11.1, 12.24, 7.25)	a_1,b_3,c_1,d_1	$(-18.2 \pm 0.1, -11.5 \pm 0.6)$	$(-17.3 \pm 0.2, -12.0 \pm 0.3)$	$(-14.8 \pm 0.1, -12.4 \pm 0.2)$	$(-14.4 \pm 0.1, -12.7 \pm 0.3)_{d\leq 22.5\,\mathrm{pc}}$
	mwp14	8.122	27	(11.1, 12.24, 7.25)	a_1,b_4,c_1,d_1	$(-18.2 \pm 0.1, -11.4 \pm 0.3)$	$(-17.4 \pm 0.2, -11.8 \pm 0.3)$	$(-14.8 \pm 0.1, -12.4 \pm 0.2)$	$(-14.2 \pm 0.1, -12.8 \pm 0.2)$
	mwp14	8.7	27	(11.1, 12.24, 7.25)	a_1,b_5,c_1,d_1	$(-18.3 \pm 0.2, -11.4 \pm 0.3)$	$(-17.5 \pm 0.3, -11.4 \pm 0.5)$	$(-14.9 \pm 0.1, -12.3 \pm 0.2)$	$(-14.4 \pm 0.1, -12.7 \pm 0.1)$
Sun velocity	mwp14	8.3	27	(10.1, 4.0, 6.7)	a_1,b_1,c_1,d_2	$(-18.3 \pm 0.1, -11.4 \pm 0.3)$	$(-17.4 \pm 0.2, -11.9 \pm 0.3)$	$(-14.8 \pm 0.1, -12.4 \pm 0.2)$	$(-14.3 \pm 0.1, -12.8 \pm 0.2)$
	mwp14	8.3	27	(10.0, 5.25, 7.17)	a_1,b_1,c_1,d_3	$(-18.3 \pm 0.1, -11.4 \pm 0.3)$	$(-17.4 \pm 0.2, -11.9 \pm 0.3)$	$(-14.7 \pm 0.1, -12.4 \pm 0.2)$	$(-14.3 \pm 0.1, -12.8 \pm 0.2)$
	mwp14	8.3	27	(10.0, 15.4, 7.8)	a_1,b_1,c_1,d_4	$(-18.3 \pm 0.1, -11.4 \pm 0.2)$	$(-17.4 \pm 0.3, -11.9 \pm 0.3)$	$(-14.9 \pm 0.1, -12.4 \pm 0.2)$	$(-14.3 \pm 0.1, -12.8 \pm 0.2)$
Sun height	mwp14	8.3	0	(11.1, 12.24, 7.25)	a_1,b_1,-,d_1	$(-18.4 \pm 0.2, -11.4 \pm 0.2)$	$(-17.6 \pm 0.2, -11.4 \pm 0.8)$	$(-14.9 \pm 0.1, -12.4 \pm 0.1)$	$(-14.4 \pm 0.1, -12.8 \pm 0.2)$
	mwp14	8.3	50	(11.1, 12.24, 7.25)	a_1,b_1,-,d_1	$(-18.2 \pm 0.1, -11.5 \pm 0.3)$	$(-17.4 \pm 0.2, -11.9 \pm 0.3)$	$(-14.8 \pm 0.1, -12.4 \pm 0.2)$	$(-14.3 \pm 0.1, -12.8 \pm 0.2)$
MW's potential	McMillan17**	8.2	20.8	(11.1, 12.24, 7.25)	a_2,a_2,c_2,d_1	$(-18.2 \pm 0.1, -11.4 \pm 0.2)$	$(-17.3 \pm 0.2, -11.9 \pm 0.3)$	$(-14.8 \pm 0.1, -12.3 \pm 0.2)$	$(-14.1 \pm 0.1, -12.8 \pm 0.2)$
	Irrgang13I***	8.4	20.8	(11.1, 12.24, 7.25)	a_3,a_3,c_2,d_1	$(-18.2 \pm 0.1, -11.5 \pm 0.3)$	$(-17.3 \pm 0.2, -11.8 \pm 0.3)$	$(-14.8 \pm 0.1, -12.4 \pm 0.2)$	$(-14.3 \pm 0.1, -12.8 \pm 0.3)$
Mixed	mwp14	8.122	20.8	(11.1, 12.24, 7.25)	a_1,b_4,c_2,d_1	$(-18.3 \pm 0.1, -11.5 \pm 0.3)$	$(-17.4 \pm 0.2, -12.0 \pm 0.3)$	$(-14.8 \pm 0.1, -12.4 \pm 0.2)$	$(-14.2 \pm 0.1, -12.9 \pm 0.2)$
	mwp14	8.122	20.8	(10.0, 15.4, 7.8)	a_1,b_4,c_2,d_4	$(-18.3 \pm 0.1, -11.5 \pm 0.3)$	$(-17.4 \pm 0.3, -12.0 \pm 0.1)$	$(-14.9 \pm 0.1, -12.4 \pm 0.2)$	$(-14.2 \pm 0.1, -12.9 \pm 0.2)$

Notes. The time intervals for the encounters between the Solar System and the Radcliffe wave were calculated by varying the initial parameters of orbit integration. The investigated initial conditions include the Sun's Galactocentric distance, the Sun's velocity relative to the Local Standard of Rest, the height above the disk midplane of the Sun, and the potential of the Milky Way. The statistical errors of the time intervals are computed through Monte Carlo sampling the uncertainty distributions of the initial positions and velocities of the clusters, as well as the assumed initial parameters of the Sun. The errors for the Sun's initial parameters are taken from the given references. In cases where no encounter occurs for a given distance, the reported time range corresponds to the distance indicated as a subscript. In the Reference column, the letters *a*, *b*, *c*, and *d* refer to the Milky Way potential, Galactocentric distance, Sun height above the disk, and Sun's velocity relative to the Local Standard of Rest, respectively.
The circular velocity at the Sun's position is set to: $^{*}\, v_{\mathrm{LSR}} = 220\,\mathrm{km\,s^{-1}}$; $^{**}\, v_{\mathrm{LSR}} = 233.1\,\mathrm{km\,s^{-1}}$; $^{***}\, v_{\mathrm{LSR}} = 242\,\mathrm{km\,s^{-1}}$.

References. (a_1) Bovy (2015); (a_2) McMillan (2017); (a_3) Irrgang et al. (2013); (b_1) Gillessen et al. (2009); (b_2) Francis & Anderson (2014); (b_3) Eisenhauer et al. (2003); (b_4) GRAVITY Collaboration (2018); (b_5) Vanhollebeke et al. (2009); (c_1) Chen et al. (2001); (c_2) Bennett & Bovy (2019); (d_1) Schönrich et al. (2010); (d_2) Hogg et al. (2005); (d_3) Dehnen & Binney (1998); (d_4) Kerr & Lynden-Bell (1986).